



1 Understanding Absorption by Black Versus Brown Carbon in 2 Biomass Burning Plumes from the WE-CAN Campaign

3 Yingjie Shen¹, Rudra P. Pokhrel^{1, *}, Amy P. Sullivan², Ezra J. T. Levin^{2, *}, Lauren A. Garofalo³,
4 Delphine K. Farmer³, Wade Permar⁴, Lu Hu⁴, Darin W. Toohey⁵, Teresa Campos⁶, Emily V.
5 Fischer², Shane M. Murphy¹

6 ¹Department of Atmospheric Science, University of Wyoming, Laramie, WY 82071, USA.

7 ²Department of Atmospheric Science, Colorado State University, Fort Collins, CO 80523, USA

8 ³Department of Chemistry, Colorado State University, Fort Collins, CO 80523, USA

9 ⁴Department of Chemistry and Biochemistry, University of Montana, Missoula, MT 59812, USA.

10 ⁵Department of Atmospheric and Oceanic Sciences, University of Colorado Boulder, Boulder, CO 80309, USA

11 ⁶National Center for Atmospheric Research, Atmospheric Chemistry Division, Boulder, CO 80301, USA

12 *now at Air Pollution Control Division, Colorado Department of Public Health and Environment, Denver, CO 80246,
13 USA

14 *Corresponding author: Shane M. Murphy (shane.murphy@uwyo.edu)*

15 **Abstract.** Aerosol absorption of visible light has an important impact on global radiative forcing. Wildfires are one
16 of the major sources of light-absorbing aerosol, but there remains significant uncertainty about the magnitude,
17 wavelength dependence and bleaching of absorption from biomass burning aerosol. We collected and analyzed data
18 from 21 Western United States wildfire smoke plumes during the 2018 WE-CAN airborne measurement campaign to
19 determine the contribution of black carbon (BC), brown carbon (BrC), and lensing to the aerosol mass absorption
20 cross-section (MAC). MAC_{BC} , MAC of organics ($MAC_{BrC+lensing}$), and the MAC of water-soluble BrC ($MAC_{ws,BrC660}$)
21 are calculated using Photoacoustic Absorption Spectrometer, Single Particle Soot Photometer and Particle-into-Liquid
22 Sampler measurements. MAC_{BC660} does not change significantly with physical age, organic aerosol (OA)
23 concentration, oxygen to carbon ratio (O:C), gas-phase toluene:benzene ratio, modified combustion efficiency (MCE),
24 altitude, or temperature, and has a relatively stable average value of $10.9 \pm 2.1 \text{ m}^2 \text{ g}^{-1}$. On average, 54% of non-BC
25 absorption (23% total absorption) at 660 nm is from water-soluble BrC. $MAC_{ws,BrC660}$ is $0.06 \pm 0.04 \text{ m}^2 \text{ g}^{-1}$ while
26 $MAC_{BrC+lensing}$ is $0.11 \pm 0.06 \text{ m}^2 \text{ g}^{-1}$ at 660 nm, increasing to $0.59 \pm 0.19 \text{ m}^2 \text{ g}^{-1}$ at 405 nm. $MAC_{BrC+lensing}$ is constant
27 with physical age and MCE, but increases slightly with increasing O:C or decreasing toluene:benzene, while total
28 absorption (normalized to CO) slightly decreases with increasing O:C or decreasing toluene:benzene due to decreasing
29 OA. No evidence of BrC bleaching is observed. Comparison to commonly used parameterizations, modeling studies,
30 and the FIREX-AQ observations suggest model overestimation of absorption is likely due to incorrect BrC refractive
31 indices. Quantification of significant brown carbon in the red wavelengths and the stability of MAC_{BC} , the observation
32 of minimal bleaching, and the observation of changes in OA with O:C and toluene:benzene markers all serve as
33 important constraints on aerosol absorption in regional and global climate models.

34



35 1 Introduction

36 Atmospheric aerosol impact the climate system by directly scattering and absorbing solar radiation, by
37 indirectly changing cloud properties, and through deposition that changes the surface albedo (McConnell et al., 2007;
38 Sarangi et al., 2020). Biomass burning injects a large amount of primary organic aerosol (POA), secondary organic
39 aerosol (SOA) and black carbon (BC) into the atmosphere every year. BC is somewhat poorly defined but is generally
40 considered to be insoluble and refractory and includes a variety of materials such as char, biochar, charcoal, elemental
41 carbon (EC), and soot (Wei et al., 2013). Although it only represents a small fraction of aerosol mass, BC has a
42 significant impact on the global energy budget due to its ability to strongly absorb solar radiation. While still important,
43 positive radiative forcing of BC is lower in IPCC AR6 (2022) than in IPCC AR5 (2013). Bond et al. (2013) estimated
44 the direct radiative forcing for BC from 1750 to 2005 at the top of the atmosphere to be $+0.71 \text{ W m}^{-2}$, with an
45 uncertainty of 90% while the latest IPCC AR6 (2022) estimates effective radiative forcing for BC from 1750 to 2019
46 to be $+0.11 (-0.2 \sim +0.42) \text{ W m}^{-2}$. It is important to note that AR5 reported direct radiative forcing while AR6 reports
47 effective radiative forcing. While BC is emitted from nearly all combustion processes, the largest global source of BC
48 is thought to be biomass burning (Bond et al., 2013). Organic aerosol (OA) also absorbs visible light, but its absorption
49 strongly depends on the wavelength of light (Kirchstetter and Novakov, 2004). Non-BC light absorbing organic
50 compounds are often called brown carbon (BrC) and they are usually co-emitted with BC or formed by secondary
51 chemistry in biomass burning plumes (Andreae and Gelencsér, 2006). Unlike BC, which absorbs light from the UV
52 to the IR, BrC absorption sharply increases in the UV and shorter visible portions of the spectrum and has been
53 historically considered to be almost transparent near the red wavelengths (Andreae and Gelencsér, 2006; Bahadur et
54 al., 2012; Liu et al., 2020). Wildfires in the Western U.S. have increased in recent decades (Westerling et al., 2006;
55 Burke et al., 2021), and will continue increasing according to model predictions (Yue et al., 2013; Hurteau et al., 2014;
56 Ford et al., 2018; Neumann et al., 2021). Therefore, quantitative studies of the radiative effects caused by BC and BrC
57 emitted from wildfires are crucial for a better understanding of future climate and essential to improve climate models.

58 The large uncertainty in the radiative forcing from BC is caused both by uncertainties in emissions and by
59 uncertainty in properties that affect its optics, such as size distribution, morphology, refractive index, and mixing state
60 (Bond et al., 2006; Kleinman et al., 2020; Brown et al., 2021). For wildfires, most of the aerosol mass is organic
61 (Garofalo et al., 2019). When BC is internally mixed with OA, the BC is coated by other absorbing or non-absorbing
62 materials that cause more photons to interact with the BC core, and therefore enhance the absorption of the BC core.
63 This process is often called the lensing effect even though geometric lensing is not actually happening at these sizes
64 (Fuller et al., 1999). The absorption enhancement caused by the lensing effect is defined as the ratio of the absorption
65 cross-section of a coated BC particle to that of an equivalent uncoated BC particle (Lack and Cappa, 2010). Laboratory
66 experiments have shown a strong absorption enhancement of BC by a factor of two or more (Schnaiter et al., 2003;
67 Schnaiter et al., 2005; Bond and Bergstrom, 2006; Bond et al., 2006; Peng et al., 2016). While observations of
68 absorption enhancement from ambient BC vary widely in field studies due to variations in coating thickness, coating
69 material, source type, or methodological differences, it is often much lower than laboratory values (Liu et al., 2015,
70 2017; Cappa et al., 2012, 2019; Healy et al., 2015; Krasowsky et al., 2016). Cappa et al. (2019) summarized absorption



71 enhancements observed at the red end of the visible spectrum from 10 studies including ambient measurements, source
72 sampling, and lab experiments. The absorption enhancement reported by those measurements ranged from 1.1 to 2.8.
73 Three methods (referred to henceforth as core-shell Mie theory, thermal denuder, and mass absorption cross-
74 section) can be used to obtain estimates of absorption enhancement. Numerical solutions to Mie theory (Bohren and
75 Huffman, 1983) have been used to model aerosol absorption for many years and can be adapted into a core-shell
76 model, which is a simplified version of the complex mixing states in real atmospheric particles (Chylek et al., 2019).
77 The core-shell model assumes particles are concentric spheres, where BC acts as a core and the other materials
78 (typically organics) act as a shell. This model can simulate the absorption enhancement with geometric and optical
79 inputs (i.e., shell thickness, particle radius, refractive index). However, the assumptions made by Mie theory may have
80 significant errors for irregular particles, often found in fresh soot particles and when mixed BC and organics are not
81 concentric spheres. A thermodenuder can be used to remove volatile coating materials by heating them to a
82 temperature from 250 – 400 °C. The ratio of the absorption coefficient measured in ambient air and measured after
83 passing particles through the thermodenuder gives an empirical absorption enhancement. Liu et al. (2015) utilized a
84 thermodenuder to find the average absorption enhancement at 405 nm and 781 nm to be 1.3 and 1.4, respectively, in
85 the UK during winter. Pokhrel et al. (2017) utilized a photoacoustic absorption spectrometer (PAS) with a
86 thermodenuder and showed that absorption enhancement determined in this manner depends on fuel type and
87 combustion conditions, with absorption enhancements ranging from 0.92 to 1.43 at 660 nm and reaching a maximum
88 of 5.6 at 405 nm. However, a thermodenuder cannot always remove coating materials completely and thus can lead
89 to underestimates of absorption enhancement. The mass absorption cross section of BC (MAC_{BC}) is another way to
90 describe the absorbing ability of BC containing particles by describing the absorption per unit mass of BC. MAC_{BC}
91 can be a fundamental input in climate models to convert mass concentration into absorption coefficients (Cho et al.,
92 2019). MAC_{BC} is the particulate absorption divided by the mass of the pure BC at the same wavelength. In this way,
93 the calculated MAC_{BC} will include absorption of the BC core, the absorption and absorption enhancement caused by
94 the coating material. Unfortunately, MAC_{BC} in the ambient atmosphere continues to be not well understood due to the
95 lack of field measurements and instrumental limitations. The atmospheric aging processes on BC can introduce
96 uncertainties on its absorption. Bond and Bergstrom (2006) suggested a MAC_{BC} of $7.5 \pm 1.2 \text{ m}^2 \text{ g}^{-1}$ at 550 nm for fresh
97 BC. Subramanian et al. (2010) reported a MAC_{BC} of $10.9 \pm 2.1 \text{ m}^2 \text{ g}^{-1}$ at 660 nm and $13.1 \text{ m}^2 \text{ g}^{-1}$ at 550 nm over Mexico
98 City when using a single particle soot photometer (SP2) and the filter-based particle soot absorption photometer (PSAP)
99 instrument during airborne measurements. Krasowsky et al. (2016) reported a MAC_{BC} enhancement of 1.03 ± 0.05 due
100 to the coatings on BC. Zhang et al. (2017) found a MAC_{BC} with a mean of $10 \text{ m}^2 \text{ g}^{-1}$ and a standard deviation of 4 m^2
101 g^{-1} at 660 nm by using both SP2 and PSAP measurements. Cho et al. (2019) summarized MAC_{BC} estimated from more
102 than 10 studies in East and South Asia in both ambient conditions and laboratory experiments, and the values ranged
103 from 4.6 to $11.3 \text{ m}^2 \text{ g}^{-1}$.

104 To improve the understanding of the evolution of light-absorbing aerosol from biomass burning, smoke from
105 21 wildfires in the Western United States were measured near their sources and downwind onboard the NSF/NCAR
106 C-130 aircraft during the Western Wildfire Experiment for Cloud Chemistry, Aerosol Absorption and Nitrogen (WE-
107 CAN) campaign. This campaign represented one of the first airborne attempts to fully characterize Western U.S.



108 wildfires from several different fuel types, locations, and fire stages (flaming vs. smoldering). This paper presents
109 novel observations about the absorbing properties of the aerosol and compares these observations to modeling studies
110 conducted with the WE-CAN data and to results from the Fire Influence on Regional to Global Environment – Air
111 Quality (FIREX) study conducted in 2019 (Zeng et al., 2021).

112 2 Experimental Method

113 This work relies on measurements made during the WE-CAN field campaign, which sampled smoke emitted
114 by wildfires across the Western U.S. using the NSF/NCAR C-130 research aircraft. The goal of the campaign was to
115 make detailed observations of the physical, chemical, and optical evolution of aerosol in western wildfire smoke and
116 its impact on climate, air quality, weather, and nutrient cycles. The WE-CAN field campaign consisted of 19 research
117 flights that took place from Jul. 24 – Sep. 13, 2018. Data from 13 flights were analyzed in this study. The flight path
118 and dominant wildfire for each of these flights are shown in Fig. 1.

119

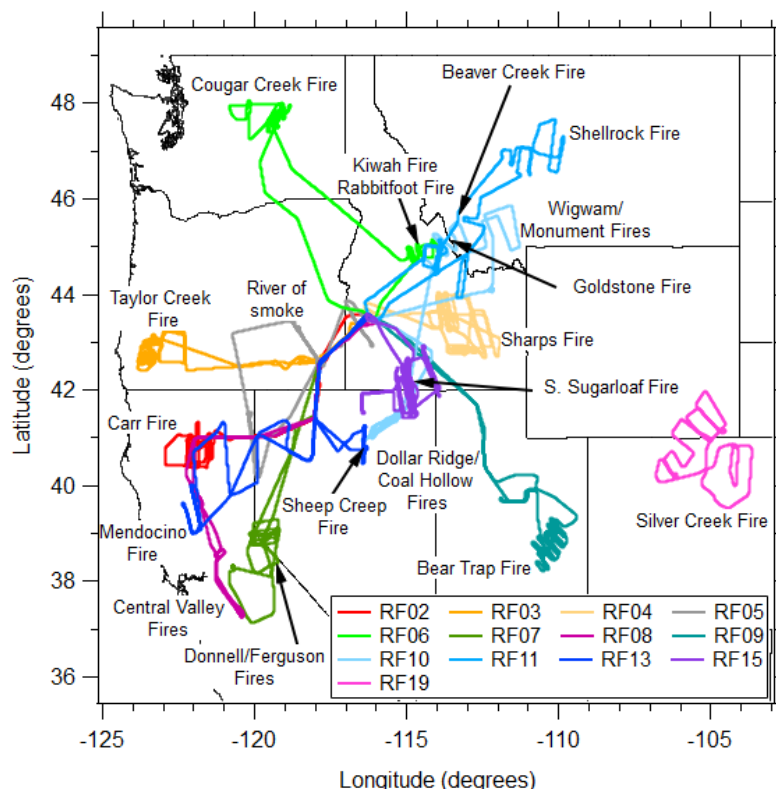


Figure 1: Flight paths and the sampled wildfires for the WE-CAN flights analyzed in this paper.



120 2.1 Instrumentation

121 The following instruments are a subset of those flown during the WE-CAN campaign and are utilized in this
122 work. The full WE-CAN dataset is archived at https://data.eol.ucar.edu/master_lists/generated/we-can. All aerosol
123 instruments utilized in this paper, except the PILS, used pulled air from the same Solid Diffuser Inlet (SDI) inlet. The
124 PILS sampled from a Submicron Aerosol Inlet (SMAI) (Craig et al., 2013a, 2013b, 2014; Moharreri et al., 2014).

125 2.1.1 Photoacoustic Absorption Spectrometer (PAS)

126 Aerosol absorption coefficients were measured with the multi-wavelength PAS built by the University of
127 Wyoming (Foster et al., 2019), based on the design of Lack et al. (2012b). A PAS can directly measure the absorption
128 coefficient of dry aerosol. The PAS represents the only way to directly measure aerosol absorption other than the
129 photothermal interferometer (PTI, Sedlacek, 2007), which measures the change in the refractive index of the air near
130 particles caused by absorption. Briefly, when modulated laser light (at the resonant frequency of the cell) is absorbed
131 by the aerosol, pressure waves are created and amplified by the cavity then detected by two microphones (Lack et al.,
132 2006; Foster et al., 2019). The PAS used here has four cells that measure the aerosol absorption coefficient from dry
133 air at 405 nm and 660 nm and thermally denuded air at 405 nm and 660 nm. The denuder was set to 300°C, with the
134 goal of evaporating volatile organic aerosol which might have a potential impact on light absorption. However,
135 absorption from the denuded channels was not used in this study, because the absorption enhancement calculated
136 using the thermodenuder approach is much smaller than the approach taking the ratio of MAC_{BC} to $MAC_{BC-core}$, and
137 we believe the discrepancy is due to the presence of significant residual organic material after denuding. Two NO_x
138 denuders coated with potassium hydroxide, guaiacol and methanol were installed on the PAS in front of the inlet to
139 remove the absorption from gas-phase NO_2 (Williams and Grosjean 1990). A 3 LPM $PM_{2.5}$ cyclone (URG-2000-
140 30ED) was used on the PAS in front of the inlet to provide a $PM_{1.0}$ cut. In addition, a Nafion drier (Purma Pure PD-
141 100T-24MPS) with 100 tubes was installed on the inlet system to dry sample to a relative humidity below 30%. The
142 uncertainty in the absorption coefficient measured by the PAS mainly comes from the calibration technique, in which
143 the highly absorbing substance Regal Black and the CAPS PM_{SSA} were utilized (Foster et al., 2019). The PAS was
144 routinely calibrated (after each flight or every other day if there was a flight everyday) during WE-CAN with an
145 accuracy of +/- 10%.

146 The PAS microphone shows a pressure-dependent response to pressure. To account for this behavior, we
147 performed pressure-dependent calibration of the PAS where the instrument pressure (both PAS and CAPS PM_{SSA})
148 was dropped stepwise by ~50 torr from ambient to ~300 torr (typical minimum pressure level during WE-CAN). A
149 calibration was performed at each pressure step and the calibration constants were fitted with pressure to get a change
150 in calibration at a desired pressure. Pressure-dependent calibrations were repeated pre and post-campaign to capture
151 variability.

152 Aerosol optical properties (absorption and extinction) were converted to standard temperature and pressure
153 (STP, 1 atm, 0°C) before data were uploaded. We used temperature and pressure measured by the PAS and CAPS
154 PM_{SSA} to convert optical properties to STP. For absorption, the sample temperature measured by the PAS RH sensor



155 (Vaisala RH probe) and the pressure measured by the temperature and pressure sensor of the CAPS PM_{SSA} were used.
156 Whereas for extinction, temperature and pressure measured by the CAPS PM_{SSA} were used.

157 **2.1.2 Cavity-Attenuated Phase Shift Spectrometer (CAPS PM_{SSA})**

158 After pulling through the NO_x denuder, the PM_{1.0} cyclone, and the Nafion drier in front of the PAS inlet, the
159 sampled air entered through the Aerodyne CAPS PM_{SSA_450} and CAPS PM_{SSA_660} to measure the aerosol scattering
160 and extinction coefficients at 450 nm and 660 nm, respectively. CAPS PM_{SSA} instruments measure extinction by
161 utilizing the cavity attenuated phase shift spectroscopy and measure scattering with an integrating sphere (Onasch et
162 al., 2015). Ammonium sulfate particles were used to calibrate the scattering channel of the CAPS PM_{SSA} during WE-
163 CAN with an accuracy of +/- 3%.

164 **2.1.3 Particle-into-Liquid Sampler (PILS) systems**

165 BrC absorption and water-soluble organic carbon (WSOC) were measured by a Particle-into-Liquid Sampler
166 (PILS) system (Sullivan et al., 2022). The PILS continuously collects ambient particles into purified water and
167 provides a liquid sample with the aerosol particles dissolved in it for analysis (Orsini et al., 2003). The size-cut for the
168 PILS was provided by a nonrotating microorifice uniform deposit impactor (MOUDI) with a 50% transmission
169 efficiency of 1 μm (aerodynamic diameter) at 1 atmosphere ambient pressure (Marple et al., 1991). The total airflow
170 for the PILS was approximately 15 LPM. Upstream of the PILS was an activated carbon parallel plate denuder
171 (Eatough et al., 1993) to remove organic gases. In addition, a valve was manually closed periodically for 10 min
172 diverting the airflow through a Teflon filter before entering the PILS allowing for background measurements. The
173 liquid sample obtained from the PILS was pushed through a 0.2 μm PTFE liquid filter by a set of syringe pumps to
174 ensure insoluble particles were removed. The flow was then directed through a liquid waveguide capillary cell (LWCC)
175 and Total Organic Carbon (TOC) Analyzer for near real-time measurement of BrC absorption and WSOC,
176 respectively. More details and a schematic illustration can be found in Zeng et al. (2021).

177 For the absorption measurement, a 2.5 m path-length LWCC (World Precision Instruments, Sarasota, FL)
178 was used. A dual deuterium and tungsten halogen light source (DH-mini, Ocean Optics, Largo, FL) and absorption
179 spectrometer (FLAME-T-UV-VIS, Ocean Optics, Largo, FL) were coupled to the LWCC via fiber optic cables.
180 Absorption spectra were recorded using the Oceanview Spectroscopy Software over a range from 200 to 800 nm. The
181 wavelength-dependent absorption was calculated following the method outlined in Hecobian et al. (2010). For this
182 study, a 16 s integrated measurement of absorption with a limit of detection (LOD) of 0.1 Mm⁻¹ was obtained (Sullivan
183 et al., 2022).

184 For the WSOC measurement, a Sievers Model M9 Portable TOC Analyzer (Suez Waters Analytical
185 Instruments, Boulder, CO) was used. This analyzer works by converting the organic carbon in the liquid sample to
186 carbon dioxide through chemical oxidation involving ammonium persulfate and ultraviolet light. The carbon dioxide
187 formed was then measured by conductivity. The increase in conductivity observed was proportional to the amount of
188 organic carbon in the liquid sample. The analyzer was run in turbo mode providing a 4 s integrated measurement of
189 WSOC with a LOD of 0.1 μg C/m³ (Sullivan et al., 2022).



190 **2.1.4 Single Particle Soot Photometer (SP2)**

191 Refractory black carbon (rBC) number and mass concentrations were measured with a Single Particle Soot
192 Photometer (SP2; Droplet Measurement Technologies) which uses a continuous, 1064 nm Nd:YAG laser to heat
193 absorbing material, primarily rBC, to its vaporization temperature and measures the resulting incandescence (Schwarz
194 et al., 2006). Similar to the CAPS PM_{SSA}, the sampled air was sent through the NO_x denuder, PM_{1.0} cyclone, and
195 Nafion drier in front of the PAS inlet before it went to the SP2. The SP2 was calibrated with PSL and size-selected
196 fullerene soot. On the C-130, the SP2 sample line was diluted with HEPA-filtered, pressured ambient air that was
197 passed through a mass flow controller to prevent signal saturation. During post-processing the data was corrected for
198 dilution back to ambient concentrations then to STP.

199 **2.1.5 Ultra-High Sensitivity Aerosol Spectrometer (UHSAS)**

200 Particle number concentration was measured by a rack-mounted Ultra-High Sensitivity Aerosol Spectrometer
201 (UHSAS). The flow rate of the rack-mounted UHSAS can be manually lowered by the in-flight operator when the
202 aircraft flew across smoke plumes, so that the UHSAS can stay within its optimum concentration measurement range
203 (Sullivan et al., 2022). The UHSAS was calibrated with ammonium sulfate. The particle mass concentration was
204 calculated by applying these size bins and multiplying by a particle density of 1.4 g cm⁻³ (Sullivan et al., 2022).

205 **2.1.6 Proton-Transfer-Reaction Time-of-Flight Mass Spectrometer (PTR-ToF-MS)**

206 The University of Montana proton-transfer-reaction time-of-flight mass spectrometer (PTR-ToF-MS 4000,
207 Ionicon Analytik) was utilized to report the VOC mixing ratios during WE-CAN (Permar et al., 2021). Only the
208 toluene and benzene mixing ratio derived from the PTR-ToF-MS were used in this work; their overall uncertainty is
209 < 15%. More details of the operation, calibration, and validation on the PTR-ToF-MS during WE-CAN can be found
210 in Permar et al. (2021).

211 **2.1.7 High-Resolution Aerosol Mass Spectrometry (HR-AMS)**

212 Organic aerosol (OA) was detected by the high-resolution aerosol mass spectrometry (HR-AMS; Aerodyne
213 Inc.). The description of the AMS operation during WE-CAN can be found in Garofalo et al. (2019). The atomic
214 oxygen-to-carbon ratios (O:C) and organic mass-to-organic carbon ratio (OM:OC) used in this work were determined
215 via the improved ambient elemental analysis method for the AMS (Canagaratna et al., 2015). Average (integrated)
216 elemental ratios were obtained by averaging (integrating) elemental masses of carbon, hydrogen, and oxygen and
217 recalculating elemental ratios.

218 **2.1.8 Quantum Cascade Laser (QCL) and Picarro Cavity Ring-Down spectrometer (Picarro)**

219 The carbon monoxide (CO) mixing ratio was measured by both an Aerodyne quantum cascade laser
220 instrument (CS-108 miniQCL) and a Picarro cavity ring-down spectrometer (G2401-m WS-CRD) (Garofalo et al.,
221 2019). Because the QCL has better precision than the Picarro instrument, CO measurements from the QCL were
222 preferentially used. However, CO measurements from the Picarro CO data were used for RF10 and RF13, because



223 the CO-QCL was not operated during those two flights. The carbon dioxide (CO₂) mixing ratio was also determined
224 from the Picarro.

225 **2.2 Plume Physical Age**

226 The physical age of the plume was calculated by dividing the distance the plume was sampled from the fire
227 source by the in-plume average wind speed. The average wind speed was measured on the NSF/NCAR C-130 aircraft
228 during each plume pass. The distance was estimated by using the longitude and latitude of the geometric center of the
229 plume measured on the NSF/NCAR C-130 and the fire location provided by the U.S. Forest Service. These same
230 plume ages were used by Garofalo et al. (2019), Peng et al. (2020), Lindaas et al. (2021), Permar et al. (2021), and
231 Sullivan et al. (2022).

232 **2.3 Plume Integration Method**

233 During the WE-CAN campaign, both the SP2 and PILS had a significant hysteresis compared to other
234 instruments. In the SP2 this is because the sampled air was diluted with particle-free ambient air at various ratios to
235 prevent signal saturation. In the PILS this is because of the retention effect of liquid on the wetted component or within
236 dead volumes (Zeng et al., 2021). Therefore, it was most accurate to integrate properties across airborne transects of
237 wildfire plumes to avoid the impact of instrument hysteresis and measurement noise that can dramatically impact
238 instantaneous ratios. Pseudo-Lagrangian sampling was used during the flights for the WE-CAN campaign, the C-130
239 aircraft repeatedly crossed the smoke plume from a particular fire by traveling perpendicular to the prevailing winds,
240 crossing the plume, turning, then crossing the plume again further downwind. In this work, we manually identified
241 plume edges based on the inflection point when CO concentrations stopped rapidly changing as we entered and exited
242 the smoke plume. The outside of plume measurement periods had CO mixing ratios from 100 - 300 ppbv. The lowest
243 10% of each variable from outside plume segments were set to be the background of that variable. If the time between
244 two consecutive outside plume segments was larger than 20 s and the highest CO mixing ratio was 100 ppbv higher
245 than the outside plume CO criteria, this segment was chosen as a plume. The start and end point of each plume was
246 slightly adjusted manually based on the CO mixing ratio to make sure the entire plume was covered. A different start
247 and end point for the SP2 and PILS was adjusted manually based on the rBC mass concentrations and WSOC,
248 respectively.

249 **2.4 Absorption Enhancement and Mass Absorption Cross-section**

250 Absorption enhancement (E_{abs}) is the ratio of the absorption of the whole particle (including BC core and
251 coating materials) to the absorption of the BC core (Lack and Cappa, 2010). E_{abs} at a specific wavelength ($E_{abs,\lambda}$)
252 was calculated in this study by Eq. 1:

$$E_{abs,\lambda} = \frac{\beta_{Total,\lambda}}{M_{BC} * MAC_{BC,core,\lambda}} \quad (Eq. 1)$$

253

254 where $\beta_{Total,\lambda}$ is the total absorption coefficient at a wavelength of λ nm measured by the PAS, M_{BC} is the mass



255 concentration of BC measured by the SP2, and $MAC_{BC_core_λ}$ is the MAC of BC core (without any other coating
 256 material) at $λ$ nm, which is set to be $6.3 \text{ m}^2 \text{ g}^{-1}$ at 660 nm (Bond and Bergstrom, 2006; Subramanian et al., 2010).

257 MAC_{BC} at $λ$ nm was calculated following Eq. 2:

$$258 \quad MAC_{BC_λ} = \frac{\beta_{Total_λ}}{M_{BC}} \quad (Eq. 2)$$

259 MAC_{BC} is utilized more often in this study than E_{abs} because there is not a widely accepted MAC for BC emitted from
 260 wildfire. MAC of BrC and lensing is calculated at 405 and 660 nm (Eq. 3):

$$261 \quad MAC_{BrC+lensing_λ} = \frac{\beta_{Total_λ} - M_{BC} * MAC_{BC_core_λ}}{M_{OA}} \quad (Eq. 3)$$

262 where M_{OA} is the organic mass measured by the AMS. Again, the MAC of the BC core is set to be 6.3 and 10.2,
 263 respectively, at 660 nm and 405 nm yielding an absorption Ångström exponent (AAE, the negative slope of a
 264 logarithmic absorption coefficient against wavelength) of 0.99 for the BC core (Bond and Bergstrom, 2006;
 265 Subramanian et al., 2010; Liu, et al., 2015). It should be noted that both BrC and lensing contribute to the $MAC_{BrC+lensing}$,
 266 and cannot be separated using this approach. MAC of water-soluble BrC at 660 nm ($MAC_{ws_BrC_660}$) is calculated using
 267 Eq. 4:

$$268 \quad MAC_{ws_BrC_660} = \frac{\beta_{ws_BrC660}}{WSOC} \quad (Eq. 4)$$

269 where β_{ws_BrC660} is water-soluble light absorption and WSOC is water-soluble organic carbon mass, which are both
 270 measured by the PILS system.

271 To investigate which contributes more to absorption enhancement at 660 nm, the absorption from BrC or
 272 the lensing effect, the fractional absorption from BrC at 660 nm is calculated by Eq. 5

$$273 \quad Fractional \ Abs_{BrC} = \frac{\beta_{BrC_660}}{\beta_{Total_660} - M_{BC} * MAC_{BC_core_660}} \quad (Eq. 5)$$

274 where β_{BrC_660} is the total BrC absorption coefficient at 660 nm. This is calculated from the water-soluble light
 275 absorption provided by the PILS, where we convert absorption from water-soluble BrC to total BrC by WSOM:WSOC
 276 and OM:WSOM ratio, and correct absorption from liquid phase to particle phase via Mie theory (more details in 3.1.4,
 277 Eq. 9-10). This approach assumes that water insoluble BrC has the same refractive index as water soluble BrC. This
 278 assumption would provide a lower estimation on the BrC contribution to the total absorption because Sullivan et al.
 279 (2022) found that 45% of the BrC absorption at 405 nm in WE-CAN came from water-soluble species, and Zeng et
 280 al. (2022) found that insoluble BrC absorbs more at higher wavelengths than soluble BrC, and methanol-insoluble
 281 BrC chromophores caused 87% of the light absorption at 664 nm. β_{Total_660} is the total absorption coefficient at 660
 282 nm which is measured by the PAS, M_{BC} is the mass concentration of BC which is measured by the SP2, and
 283 $MAC_{BC_core_660}$ is the MAC of the BC core at 660 nm which is set to be $6.3 \text{ m}^2 \text{ g}^{-1}$ (Bond and Bergstrom, 2006;
 284 Subramanian et al., 2010).



285 2.5 Modified Combustion Efficiency (MCE)

286 The variation of burn condition (e.g., flaming vs. smoldering) and fuel type can cause a significant difference
287 in BC emissions and changes in aerosol properties (Akagi et al., 2011; Andreae, 2019). Burn conditions can be
288 estimated with the modified combustion efficiency (MCE), defined as Eq. 6:

$$289 \quad MCE = \frac{\Delta CO_2}{\Delta CO + \Delta CO_2} \quad (Eq. 6)$$

290 where ΔCO_2 and ΔCO are the background-subtracted CO_2 and CO mixing ratio. The background of CO_2 and CO
291 mixing ratio is obtained via the same process described in Section 2.3.

292 2.6 Absorption, Scattering and Single Scattering Albedo (SSA)

293 Plume integrated absorption and scattering were normalized (x/CO) by taking the ratio of background-
294 subtracted absorption or scattering (Δx) to the background-subtracted CO mixing ratio (ΔCO) (Eq. 7), so that the
295 changing of the normalized properties is not impacted by dilution of the plume with background air.

$$296 \quad x/CO = \frac{\Delta x}{\Delta CO} \quad (Eq. 7)$$

297 Although the CAPS PM_{SSA} provides scattering directly, the scattering is only accurate if extinction is below
298 1000 Mm^{-1} (Onasch et al., 2015). We calculated scattering by subtracting absorption measured by the PAS from
299 extinction measured by the CAPS PM_{SSA} to avoid high uncertainty caused by extremely dark plumes. Similarly, SSA
300 at a specific wavelength (λ) was also calculated by using both the PAS absorption ($\beta_{Total,\lambda}$) and CAPS PM_{SSA}
301 extinction (Ext_λ) (Eq. 8).

$$302 \quad SSA_\lambda = \frac{Ext_\lambda - \beta_{Total,\lambda}}{Ext_\lambda} \quad (Eq. 8)$$

303 3 Results and Discussion

304 3.1 Absorption of BC and BrC at Red Wavelengths

305 3.1.1 Mass Absorption Cross-Section of Black Carbon at 660 nm

306 Plume integrated MCE, MAC_{BC} at 660 nm (MAC_{BC660}) and BC:OA ratio from the 13 WE-CAN research
307 flights with clear plume transects of biomass burning plumes are shown in Fig. 2. Even fire plumes from individually
308 named fires are usually a mix of many different burning conditions, and it is hard to identify the exact source in most
309 wildfire smoke measurements, especially for well mixed plumes. Therefore flight-to-flight data is analyzed in this
310 study because each flight covered a region, and an overall behavior of absorbing aerosol from wildfire can be provided.
311 MAC_{BC660} varies between different flights with RF03 having the highest average MAC_{BC660} of $12.9 \text{ m}^2 \text{ g}^{-1}$, (median
312 MCE of 0.94, median BC:OA of 0.015) and RF10 having the lowest average MAC_{BC660} of $8.6 \text{ m}^2 \text{ g}^{-1}$, (median MCE
313 of 0.88, , median BC:OA of 0.011). The average of all plume-integrated MAC_{BC660} is $10.9 \text{ m}^2 \text{ g}^{-1}$, with a standard
314 deviation of $2.1 \text{ m}^2 \text{ g}^{-1}$. This result is similar to some other recent airborne measurements. Subramanian et al. (2010)
315 reported a MAC_{BC660} of $10.9 \pm 2.1 \text{ m}^2 \text{ g}^{-1}$ using a SP2 and PSAP operated during the MILAGRO campaign, which



316 included airborne measurements for biomass fires over Mexico. Similarly, Zhang et al. (2017) estimated a MAC_{BC660}
 317 of $10 \text{ m}^2 \text{ g}^{-1}$ utilizing both SP2 and PSAP deployed on the NASA DC-8 research aircraft for the DC3 campaign, which
 318 measured the upper tropospheric BC over the central U.S. Taylor et al. (2020) calculated a MAC_{BC655} of $12 \pm 2 \text{ m}^2 \text{ g}^{-1}$
 319 over the southeast Atlantic Ocean, using airborne measurements from a SP2 and PAS in the CLARIFY-2017 campaign.

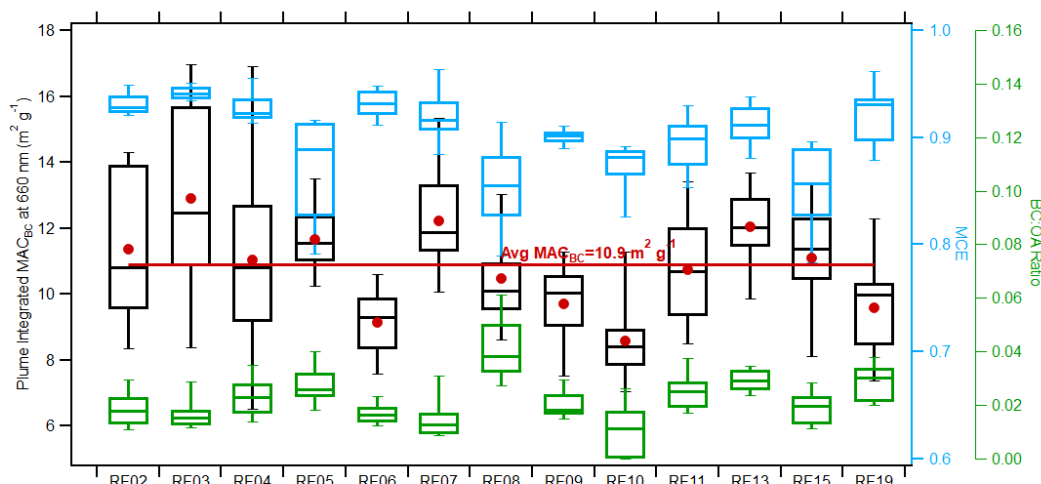


Figure 2: Box plots of plume integrated MCE (blue box), MAC_{BC660} (black box) and BC:OA (green box) for each flight. On each box the central line represents the median, the top and bottom edge represents 75% and 25%, the top and bottom whiskers represent 90% and 10%, and the red dot shows the average. The red line indicates the average value for all plume integrated MAC_{BC660} .

320 These results are encouragingly similar given the breadth of measurement techniques (PSAP is filter-based
 321 whereas PAS is a direct measurement), geographic regions (Continental U.S. for DC3, Mexico for MILAGRO,
 322 African outflow for CLARIFY) and altitude in the atmosphere (all were airborne campaigns covering a range of
 323 altitudes). If we apply $6.3 \text{ m}^2 \text{ g}^{-1}$ as the MAC of a BC core at 660 nm (Bond and Bergstrom, 2006; Subramanian et al.,
 324 2010), then the average absorption enhancement for the entire campaign is 1.7. This means the absorption of coated
 325 BC is 1.7 times higher than bare BC at 660 nm, which is close to the factor of ~ 2 reported by laboratory experiments
 326 (Schnaiter et al., 2005; Peng et al., 2016), larger than some field measurements (Cappa et al., 2012&2019; Healy et
 327 al., 2015), but close to 1.85 ± 0.45 measured by Taylor et al. (2020) in African biomass burning plumes. The similarity
 328 to the Taylor et al. (2020) result suggests global similarities in the MAC_{BC660} from aerosol emitted from wildfires.

329 The variation of MCE in different flights is caused by the different fuel sources and burning characteristics
 330 of the measured fires. Fires with high MCE tend to have more flaming combustion while those with lower MCE tend
 331 to have more smoldering combustion. Because of this, fires with different MCE may produce different coating material
 332 and thus changing MAC_{BC660} . MCE can vary in the same flight (Fig. 2), for example RF05 (mixture of multiple fire
 333 sources) and RF15 (single fire sources), because multiple fires were measured in some flights. Several other factors,
 334 such as physical age and chemical age (discussed later) also may impact MAC_{BC660} , but we first investigate if there
 335 was a clear relationship between MCE and MAC_{BC660} .



336 The comparison between plume integrated MAC_{BC660} and MCE is shown in Fig. S1. No clear relationship
337 between MAC_{BC660} and MCE can be seen from individual flights or amongst all the flights combined ($R^2=0.01$). This
338 result indicates that the combustion conditions (flaming or smoldering) does not have an easily described relationship
339 to MAC_{BC660} . This poor relation is similar to the relationship observed by Pokhrel et al. (2016). This lack of
340 relationship is likely due to the difficulty for MCE to predict aerosol properties such as BC:OA (Grieshop et al., 2009),
341 upon which effective organic aerosol absorptivity highly depends (Saleh et al., 2014).

342 3.1.2 Relationship of Bulk Optical Properties at 660 nm to Physical Age

343 Figure 3 shows the evolution of MAC_{BC660} , SSA, scattering and absorption at 660 nm versus the time since
344 emission, which will be referred to from now on as physical age. While some flights only intercepted fresh plumes
345 (for example, RF03 and RF15, with a physical age less than 200 min), others intercepted relatively old plumes (for
346 example, RF02 and RF11, with a physical age of 600 min and 800 min, respectively). To eliminate the influence of
347 dilution of particles with time, scattering and absorption are normalized by taking the ratio of the enhancement of
348 scattering or absorption above the background to the enhancement of CO concentration above the background. CO is
349 a conserved tracer that does not react on timescales relevant to these observations. No clear trend between MAC_{BC660}
350 and physical age is apparent from individual flights (Fig. 3a), linear fitting of all flights combined (black solid line)
351 gives a slope close to zero demonstrating that the absorption enhancement changes little with physical age, which is
352 consistent with the results from Subramanian et al. (2010).

353 However, SSA at 660 nm (SSA_{660}) shows a slightly increasing trend with physical age (Fig. 3b) increasing
354 from 0.94 to 0.97 in 10 hours, though the correlation is not very strong with a R^2 of 0.14. The increase of SSA_{660} is
355 partly caused by the increase of scattering at 660 nm (Fig. 3c). The particle size increases with age (Fig. S2) due to
356 coagulation of small particles and condensation of vapors. The volume mean diameter of the particles increased from
357 on average 0.18 μm to 0.34 μm across all the plumes detected. Even for each individual flight, the increasing trend in
358 particle mean diameter is clear. Another contributor to increasing SSA is the decrease in absorption at 660 nm (Fig.
359 3d) with age for most fires. Overall, the trends in SSA, absorption, and scattering with physical age are quite weak
360 with poor correlation coefficients.

361

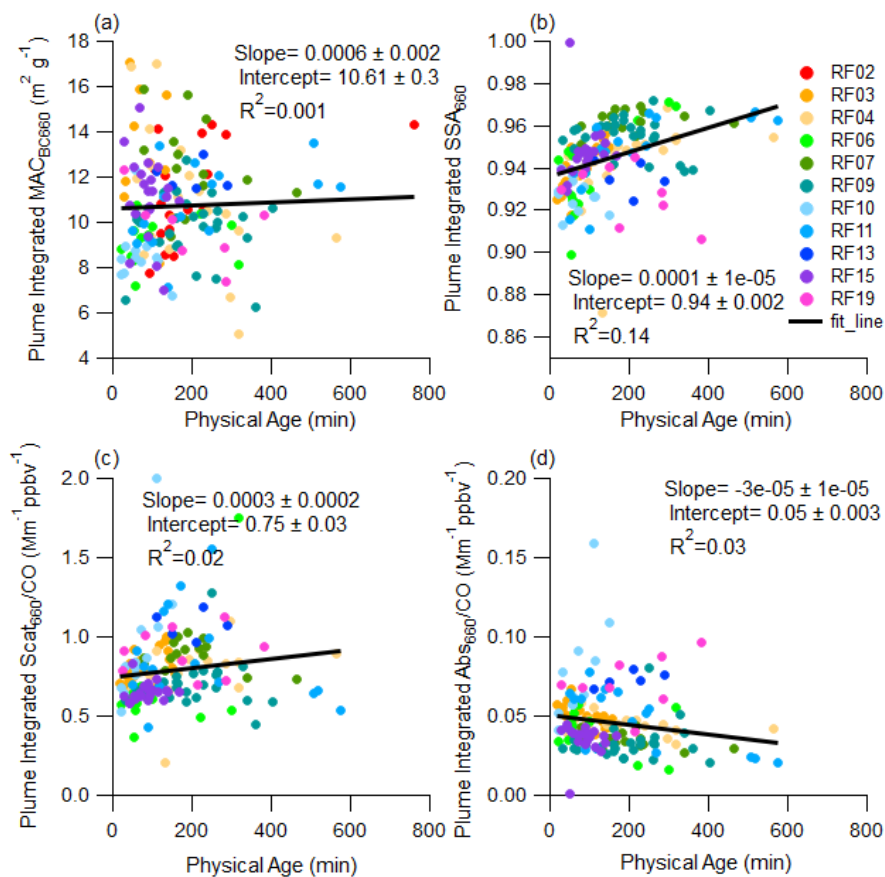


Figure 3: Time evolution of plume integrated (a) MAC_{BC660} , (b) SSA_{660} , (c) scattering, and (d) absorption at 660 nm.

362 3.1.3 Response of Optical Properties at 660 nm to Markers of Chemical Oxidation

363 MAC_{BC660} was next compared to chemical markers of oxidation, since physical age did not provide strong
364 correlations and often does not do a good job of representing oxidation and photochemical reactions that occur in
365 plumes. Organic coatings of BC cores may be removed via these reactions, or new species may condense on the BC
366 core during chemical reactions, both of which would further change the optical properties of BC. Figure 4 shows the
367 evolution of plume integrated MAC_{BC660} versus chemical clocks based on (a) the ratio of gas-phase toluene:benzene
368 and (b) the particle-phase oxygen-to-carbon (O:C) ratio. The toluene:benzene ratio decreases with photochemical
369 processing time since toluene is more reactive than benzene (Gouw et al., 2005), while the O:C ratio characterizes the
370 oxidation state of OA and typically increases with photochemical age (Aiken et al., 2008).

371 As shown in Fig. 4 the toluene:benzene ratio ranges from 0.33 to 0.88 across all flights while the O:C ratio
372 is between 0.35 and 0.72. It is difficult to discern any pattern of MAC_{BC660} changing with either marker in an individual
373 flight. However, the trends are slightly clearer after combining plumes from all the flights. From the linear fit line



374 (black solid line) to data from all flights, the negative slope of -5.7 between MAC_{BC660} and toluene:benzene ratio (Fig.
375 4a) infers that MAC_{BC660} is larger when toluene:benzene is lower, which is typically thought to indicate more extensive
376 oxidation has occurred. The positive slope of 2.2 between MAC_{BC660} and O:C ratio (Fig. 4b), supports the idea of
377 larger MAC_{BC660} with more oxidation. However, correlations are poor ($R^2 < 0.2$) and because these trends are not
378 visible within a single plume, the explanation for the trends must be either that different fires emit different O:C and
379 toluene:benzene ratios, or that the chemistry that created the observed ratios occurred before the first transect of a
380 plume. Figure S3 supports this explanation in that while there is chemical aging within flights, the O:C and
381 toluene:benzene ratios are more variable from flight to flight. For example, RF06 got more chemical aged with time,
382 but the chemical markers for RF13 were flat with time. For either mechanism, the data shows that plumes that appear
383 “older” either by photochemical aging or because of more aged appearing emissions have a slightly higher MAC_{BC660} ,
384 though the main point is that the MAC_{BC660} does not change dramatically with either physical or chemical age for the
385 observations during WE-CAN.

386 Figure 4c and 4d show that the plume-integrated mass concentration of BC (M_{BC} , from the SP2) normalized
387 by CO (the ratio of background subtracted M_{BC} to background subtracted CO) decreases with the toluene:benzene and
388 O:C ratios. One would expect a constant value of M_{BC}/CO for single plumes from an individual fire because both are
389 primary and inert. Indeed, there is no obvious decreasing of M_{BC} ($R^2 < 0.5$) within an individual flights except for
390 RF13. The decreasing of M_{BC} with markers of chemical age amongst all the flights appears to be due to the different
391 properties of the different fires near the source. Different fires tend to have different O:C ratio and toluene:benzene
392 ratios, as shown in Fig. S4. Therefore, the decreasing trend of M_{BC} with markers of chemical age is more likely caused
393 by fire-to-fire properties or rapid aging at the source rather than aging of the plume after the initial transect.

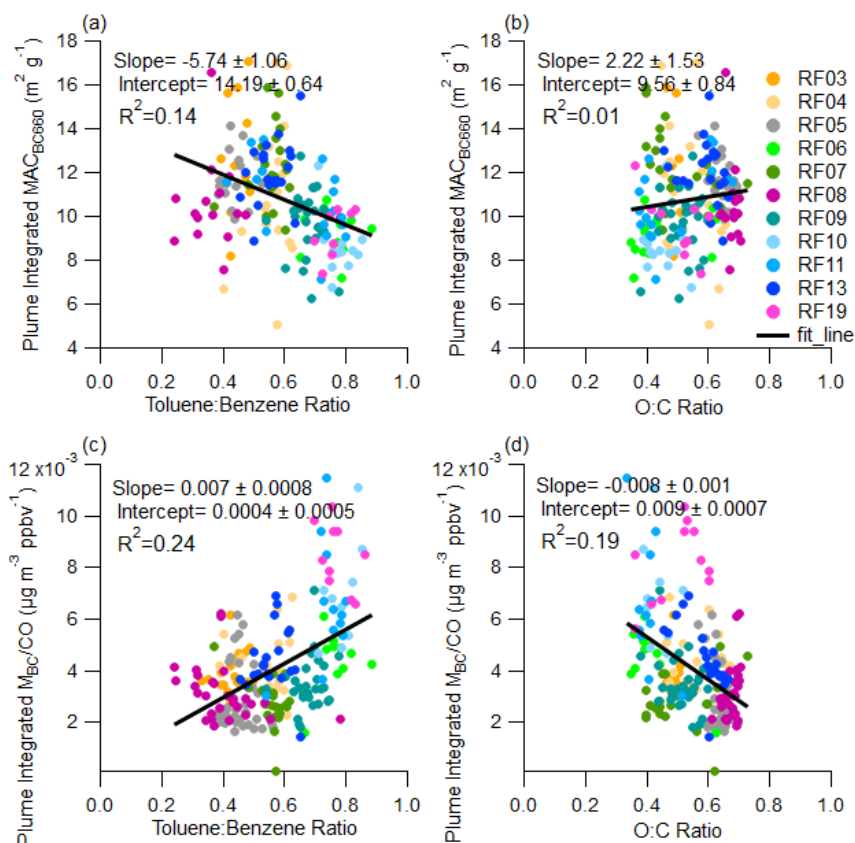


Figure 4: Plume integrated MAC_{BC660} variations with (a) toluene:benzene ratio and (b) O:C ratio; plume integrated M_{BC} variations with (c) toluene:benzene ratio and (d) O:C ratio.

394 SSA, scattering, and absorption at 660 nm are compared with the toluene:benzene ratio and O:C ratio in Fig.
395 5. There is a slight trend of increasing SSA₆₆₀ with these ratios that would correspond to more oxidized aerosol, but
396 the correlation is poor (R²=0.04). The increase of SSA₆₆₀ with markers of chemical age is consistent with the work
397 from Kleinman et al. (2020) on Western U.S. wildfire emissions, although $-\text{Log}_{10}(\text{NO}_x/\text{NO}_y)$ was used as the indicator
398 for photochemical age in their study.

399 Both scattering and absorption at 660 nm decrease with ratios corresponding to more chemical aging, which
400 suggests that the amount of absorbing material has changed. The comparison between normalized OA and these
401 markers of chemical age demonstrates that this is indeed the case. As can be seen in Fig. 5 (g-h), OA decreases with
402 increasing O:C ratio with an R² of 0.7. A similar relationship can be found between normalized WSOC chemical age
403 (Fig. 6) in that WSOC decreases with increasing O:C ratio with a R² of 0.3. However, it is key to note that this
404 correlation is not derived from individual flights and in fact is not robust in each flight and is rather due to fire-to-fire
405 variation. Figure S5 shows the correlation between normalized OA and chemical age within each fire source, which
406 shows that different fires emit different OA, and OA does not always decrease with chemical age within a single fire



407 (Kiwah fire and Rabbitfoot fire). Therefore, we believe that different OA is caused by fire properties or fast chemistry
 408 near the source, but that these markers (O:C, toluene:benzene) provide a significant correlation with the amount of
 409 organic aerosol observed in various plumes.

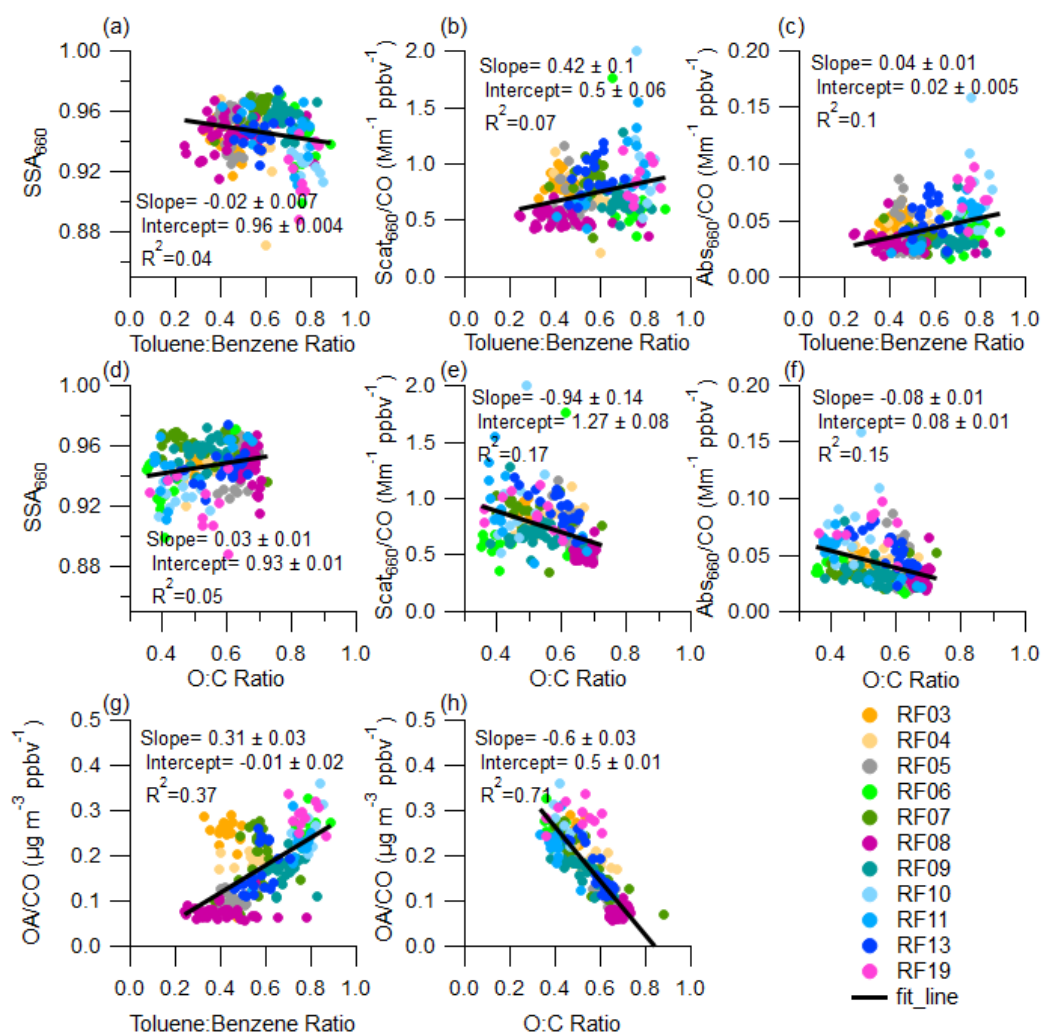


Figure 5: Plume integrated optical properties at 660 nm and normalized OA variation with chemical age. Top panels show (a) SSA, (b) Scattering, and (c) absorption variation with toluene:benzene ratio. Middle panels show (d) SSA, (e) Scattering, and (f) absorption variation with O:C ratio. Bottom panels show plume integrated normalized OA variation with (g) toluene:benzene ratio and (h) O:C ratio.

410

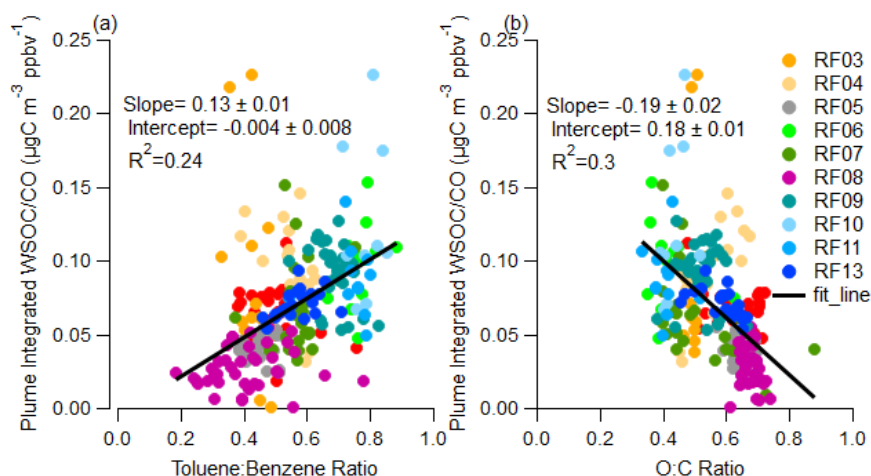


Figure 6: Plume integrated normalized WSOC variation with (a) toluene:benzene ratio and (b) O:C ratio.

411 The behavior of plume-integrated normalized OA with altitude and temperature is shown in Fig. 7 a-b. The
 412 trend is not significant, but the main reason is that for most flights we transected the plume, and caused the straight
 413 lines within the same colored marker. However, it is still clear that the smallest OA was captured in the plumes (RF08)
 414 that have highest temperature (~305 K), and larger OA tends to be observed in the colder plumes (RF19). More studies
 415 are needed to determine whether OA is evaporated in high temperature plume, but it's beyond the scope of this work.

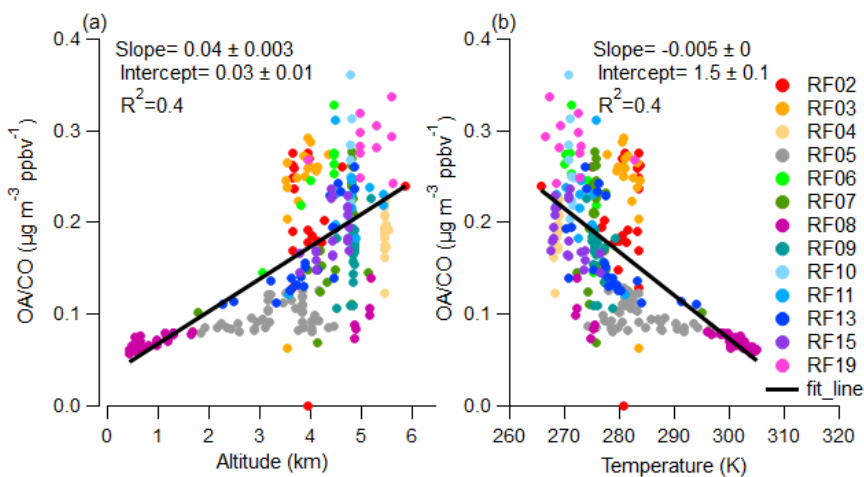


Figure 7: Plume integrated normalized OA variation with (a) altitude and (b) temperature.

416 RF05 and RF08 were chosen as case studies, to observe the optical properties of highly aged aerosol from
 417 multiple fire sources to see if the optical properties of this aerosol were similar to those observed in the plume sampling
 418 of individual fires at large chemical or physical age. RF08 was a flight through the Central Valley of California where
 419 aged smoke from multiple fires that had settled into the valley was measured while RF05 was a flight in which smoke



420 from several California fires was observed in California, Oregon and Idaho roughly 300~600 miles from the fires
421 (flightpaths are shown in Fig. 1). MAC_{BC660} , CO mixing ratio, MCE, toluene:benzene ratio, O:C ratio and SSA_{660} are
422 displayed in Fig. 8a and 8b. The mixing ratio of CO is relatively low in these aged dilute smoke plumes vs. the plumes
423 near the sources analyzed earlier. CO mixing ratio is used as an indicator of smoke when it exceeds 150 ppb. 1-minute
424 averages of MAC_{BC660} are calculated to reduce noise. Therefore, the 1-minute-averages for MCE, toluene:benzene
425 ratio and O:C ratio were also calculated, and all the negative values were removed. As shown in Fig. 8, the smallest
426 toluene:benzene ratio is ~0.35 in RF05, and is ~0.16 in RF08, while the largest O:C ratio is ~0.7 in both RF05 and
427 RF08, which indicates these two cases indeed captured plumes that appear chemically aged compared with the smallest
428 toluene:benzene ratio (0.33) and the largest O:C ratio (0.88) in near-fire measurements shown in Fig. 4.

429 In RF05 (Fig. 8a), the weighted average O:C ratio over the entire flight was 0.64, the average MCE was 0.82
430 with a standard deviation of 0.1, the toluene:benzene ratio averaged 0.45 with a standard deviation of 0.05, and the
431 SSA_{660} averaged 0.95 with a standard deviation of 0.01. MCE has a few points because all the negative values were
432 removed, where either CO or CO₂ is smaller than the background (CO < 150 ppb). MAC_{BC660} varied from 8.9 m² g⁻¹
433 to 15.7 m² g⁻¹ with an average of 11.7 m² g⁻¹ and a standard deviation of 1.38 m² g⁻¹. The reasonably large variation
434 of MCE may be caused by variability in the burn conditions of different fire sources, but the overall conclusion is that
435 these emissions, which were measured 300 to 600 miles away, have a very similar MAC_{BC660} to that of the near-source
436 flights.

437 The RF08 (Fig. 8b) results are similar to RF05, even though these emissions were smoke of mixed aged from
438 multiple fire sources in the Central Valley. The weighted average O:C ratio was 0.67 over the entire measurement,
439 average MCE was 0.84 with a standard deviation of 0.05, average toluene:benzene ratio was 0.41 with a standard
440 deviation of 0.15, and average SSA_{660} was 0.94 with a standard deviation of 0.01. MAC_{BC660} averaged 10.9 m² g⁻¹
441 with a standard deviation is 2.24 m² g⁻¹. There are several extreme values that exist in the dataset, probably because
442 of time-alignment issues caused by variation in the dilution rate of the SP2 which cannot be totally eliminated from
443 the 1-minute average. In addition, the smoke from RF08 (Fig. 8b) is split into four regions based on observed CO
444 mixing ratios, and integrated MAC_{BC660} is calculated for each region (purple star marker). Region edges are
445 represented by blue dashed lines. Region integrated MAC_{BC660} is relatively stable with an average value of 10.2 m² g⁻¹
446 ¹ and a standard deviation of 0.6 m² g⁻¹.

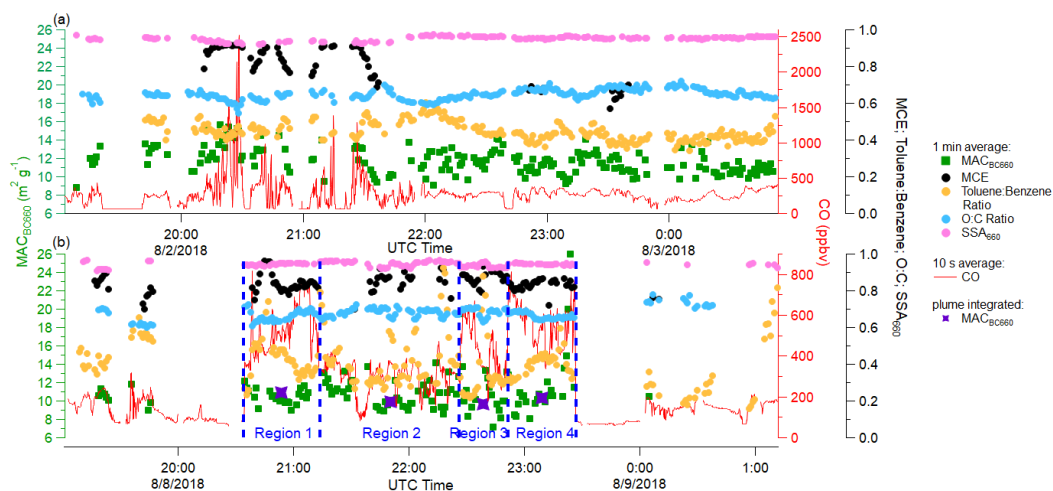


Figure 8: Time series of plume properties during (a) RF05, and (b) RF08(Central Valley of California). Different square and round markers indicate 1 min averages of different variables as shown in the legend, and the red solid line represents 10 s averages of the mixing ratio of CO. Purple stars in RF08 indicate region integrated MAC_{BC660} (individual regions are separated based on the concentration of CO, and indicated by blue dashed lines).

447 The behavior of plume-integrated MAC_{BC660} with altitude and temperature is shown in Fig. 9 a-b. MAC_{BC660}
 448 shows little correlation with altitude or temperature, even though there is a large range of both (altitude 500 m to 6
 449 km, temperature 270 K to 305 K). To assess the impact from dilution, the relation between MAC_{BC660} and ΔCO is
 450 shown in Fig. 9c. The MAC_{BC660} may decrease slightly with dilution (lower ΔCO), but the correlation is very poor.
 451 Neither altitude, temperature, or dilution appear to have a dramatic impact on the MAC_{BC660} .

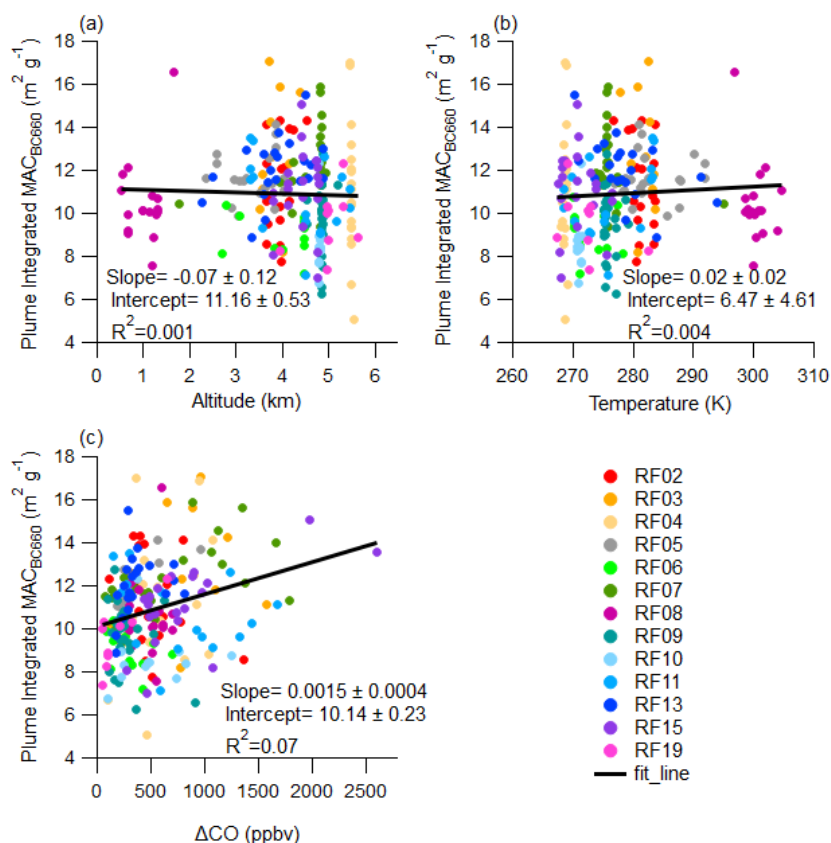


Figure 9: Plume integrated MAC_{BC660} variations with (a) Altitude, (b) Temperature, and (c) ΔCO.

452 3.1.4 Contribution of Brown Carbon Versus Lensing at 660 nm

453 Many previous studies of BrC assume that BrC does not absorb significant amounts of light at long
 454 wavelengths (532~705 nm) (Wonaschütz et al., 2009; Lack et al., 2012a; Taylor et al., 2020; Zeng et al., 2021, Zhang
 455 et al., 2022). In this study, a PILS system was used to quantify the absorption of light for water-soluble BrC at 660
 456 nm. This absorption is not likely caused by traditional BC, which is insoluble and will be removed by the 0.2 μm filter
 457 in the PILS (Peltier et al., 2007; Zeng et al., 2021).

458 One aim was to investigate if absorption enhancement at 660 nm was primarily due to the lensing effect or
 459 due to absorption from BrC. The fraction of non-BC absorption from BrC at 660 nm was calculated by Eq. 5. To
 460 convert the measured light absorption by water-soluble organics into total BrC absorption in the ambient, it had to be
 461 multiplied by two factors. The first factor converts absorption from water-soluble BrC into absorption from total BrC.
 462 This factor is obtained by taking the ratio between total particulate organic mass and water-soluble particulate organic
 463 mass (OM:WSOC). Water-soluble organic mass is calculated from the PILS WSOC data using a WSOM:WSOC
 464 (water-soluble organic mass : water-soluble organic carbon) ratio of 1.6 (Duarte et al., 2015 & 2019). Ambient organic



465 mass is measured by the AMS or calculated from the particle size distributions measured by the UHSAS assuming
 466 the particle mass all comes from organic material with a particle density of 1.4 g cm^{-3} . Both methods are used and
 467 compared in this paper. The second factor accounts for the fact that particles absorb more light than the same substance
 468 in the bulk liquid phase. Here we use Mie theory to convert absorption from BrC in aqueous solution to the absorption
 469 from BrC particles in the ambient (Liu et al., 2013; Zeng et al., 2020). The complex refractive index ($m = n + ik$) was
 470 put into a Mie code to obtain the absorption efficiency (Q), and further used to calculate the absorption coefficient by
 471 Eq. 9 (Liu et al., 2013). The real part of the refractive index (n) is set to be 1.55, and the imaginary part is calculated
 472 by using Eq. 10 (Liu et al., 2013),

$$473 \quad \beta(\lambda, D_p) = \frac{3}{2} \cdot \frac{Q \cdot WSOC}{D_p \cdot \rho} \quad (\text{Eq. 9})$$

$$474 \quad k = \frac{\rho \lambda \cdot H_2O_ \beta(\lambda)}{4\pi \cdot WSOC} \quad (\text{Eq. 10})$$

475 where λ is the wavelength, D_p is the diameter of the particle, β is absorption coefficient, Q is absorption efficiency,
 476 particle density (ρ) is set to be 1.4 g cm^{-3} , $WSOC$ is the mass concentration of WSOC ($\mu\text{gC m}^{-3}$) measured by the
 477 PILS, and $H_2O_ \beta(\lambda)$ is the water-soluble light absorption coefficient measured by PILS. The plume averaged particle
 478 size distribution was used in the calculation, then the absorption coefficient was calculated for each size bin of UHSAS
 479 to obtain the most accurate Mie factor for each plume.

480 The average OM:WSOC factor based on the UHSAS (UHSAS factor) for all the plumes is 2.36 with a
 481 standard deviation is 1.17. The averaged OM:WSOC based on the AMS (AMS factor) is 1.63 with a standard deviation
 482 of 0.74. The average Mie factor at 660 nm is 1.47 (standard deviation of 0.13), which is close to the factor of 1.36
 483 found by Zeng et al. (2022) based on FIREX data. The Mie factor at 405 nm based on the WE-CAN data is also
 484 calculated, with an average of 1.83, which is similar to the factor that Zeng et al. (2022) determined at 405 nm (1.7)
 485 based on FIREX and Liu et al. (2013) determined at 450 nm (1.9) based on measurements in Atlanta.

486 Sensitivity tests were done on these factors by choosing reasonable ranges of particle density (1.1 g cm^{-3} , 1.4
 487 g cm^{-3} and 1.7 g cm^{-3}) and WSOM:WSOC ratio (1.5, 1.6 and 1.8) (Duarte et al., 2015 & 2019; Finessi, et al., 2012;
 488 Sun et al., 2011) (Table 1). Particle density only affects the Mie factor and UHSAS factor, while WSOM:WSOC ratio
 489 affects the AMS factor and UHSAS factor. As shown in Table 1, the impact of particle density on the Mie factor (both
 490 at 660 nm and 405 nm) is negligible, WSOM:WSOC is the only component that affects the AMS factor (ranging from
 491 1.48 to 1.73), while the UHSAS factor is much more sensitive (ranging from 1.65 to 3.06) to both particle density and
 492 WSOM:WSOC. Overall, Table 1 demonstrates that none of the factors other than the UHSAS factor are sensitive to
 493 the exact parameters chosen for the calculation, giving confidence that the results presented are robust.

494 **Table 1: Average values and standard deviation of AMS factor, Mie factor at 660 nm and UHSAS factor for all the**
 495 **integrated plumes when using different particle density and WSOM:WSOC ratio. Unit of particle density is g cm^{-3} .**

Factor	Particle Density	WSOM:WSOC	Average	Standard Deviation
	N/A	1.5	1.73	0.79
AMS factor	N/A	1.6	1.63	0.74
	N/A	1.8	1.48	0.79



	1.1	N/A	1.47	0.13
Mie factor at 660 nm	1.4	N/A	1.47	0.13
	1.7	N/A	1.47	0.13
	1.1	N/A	1.83	0.89
Mie factor at 405 nm	1.4	N/A	1.83	0.89
	1.7	N/A	1.83	0.89
	1.1	1.8	1.65	0.82
UHSAS factor	1.4	1.6	2.36	1.17
	1.7	1.5	3.06	1.52

496

497

498

499

500

501

502

503

504

505

506

Figure 10 shows the time evolution of the fraction of non-BC absorption from BrC at 660 nm for the biomass burning plumes encountered during WE-CAN. Assuming a MAC of the BC core of $6.3 \text{ m}^2 \text{ g}^{-1}$, BrC contributes roughly the same amount of absorption at 660 nm as lensing (62% UHSAS method, 46% AMS method). This means that 19% (based on the AMS) to 26% (based on the UHSAS) of the total absorption at 660 nm comes from BrC. When different particle density and WSOM:WSOC ratios are considered (top and bottom whiskers, as well as red and blue dashed lines), the fraction of non-BC absorption is 43-80% for the UHSAS approach and 41-49% for the AMS approach based on different OM:OC and density. While there is considerable variability between flights, a rule of thumb that roughly half of the non-BC absorption at red wavelengths is from absorbing organic material seems reasonable. To our knowledge, this is the first attempt to differentiate between lensing and absorbing organics in the red wavelengths. This approach assumes that water insoluble BrC has the same refractive index as water soluble BrC.

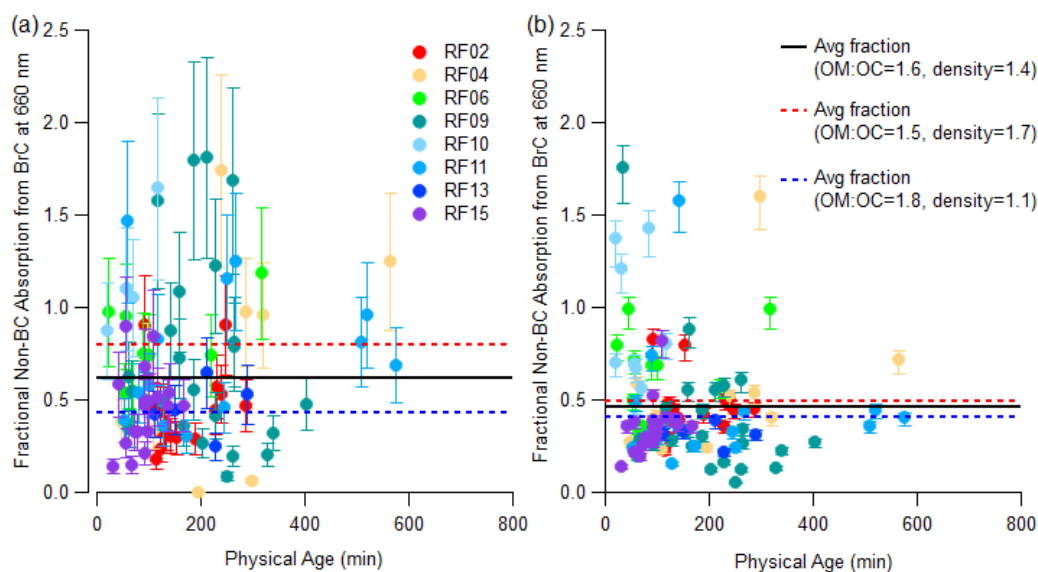


Figure 10: Time evolution of the fraction of non-BC absorption from BrC at 660 nm (a) with UHSAS and Mie factor, (b) with AMS and Mie factor. The UHSAS was not available in RF03. Markers were calculated using a density of 1.4 g cm^{-3} and WSOM:WSOC ratio of 1.6. The top whiskers represent sensitive test values using a density of 1.7 g cm^{-3} and WSOM:WSOC ratio of 1.5, while the bottom whiskers represent sensitive test values using a density of 1.1 g cm^{-3} and WSOM:WSOC ratio of 1.8. The averaged fraction of non-BC absorption from BrC from all the plumes are shown in black solid lines, while the range of this result from sensitivity tests are shown in red and blue dashed lines.

507 3.1.5 Aging of Water Soluble BrC at 660 nm

508 To further analyze the evolution of BrC at 660nm in wildfire emissions, the MAC of water-soluble BrC at
509 660 nm ($\text{MAC}_{\text{ws_BrC660}}$) was calculated by taking the ratio of water-soluble light absorption ($\beta_{\text{ws_BrC660}}$) and WSOC
510 provided by the PILS (Eq. 4). Similar to $\text{MAC}_{\text{BC660}}$, $\text{MAC}_{\text{ws_BrC660}}$ is relatively flat with physical age (Fig. 11a), with
511 an average of $0.06 \text{ m}^2 \text{ g}^{-1}$ and a standard deviation of $0.04 \text{ m}^2 \text{ g}^{-1}$, but most of the plumes measured were less than 10
512 hours old. Interestingly, the fit lines for correlations with markers of chemical age suggest that $\text{MAC}_{\text{ws_BrC660}}$ tends to
513 be larger when these markers indicate a more oxidized plume (Fig. 11 b-c), which is distinct from what has been found
514 in previous studies that BrC at shorter wavelengths decays with chemical age. The trend of increasing $\text{MAC}_{\text{ws_BrC660}}$
515 is not clear in each flight and is only observed when properties are compared between fires. While the correlation
516 coefficients are low, it can be stated that $\text{MAC}_{\text{ws_BrC660}}$ is consistently larger in more oxidized plumes and there is not
517 a decrease with increased oxidation or chemical aging. Given that all the observed smoke plumes were of similar
518 physical ages, this again leads to the idea that these properties are the result of different emissions or fast chemistry
519 that occurs before the plumes are first observed by the aircraft.

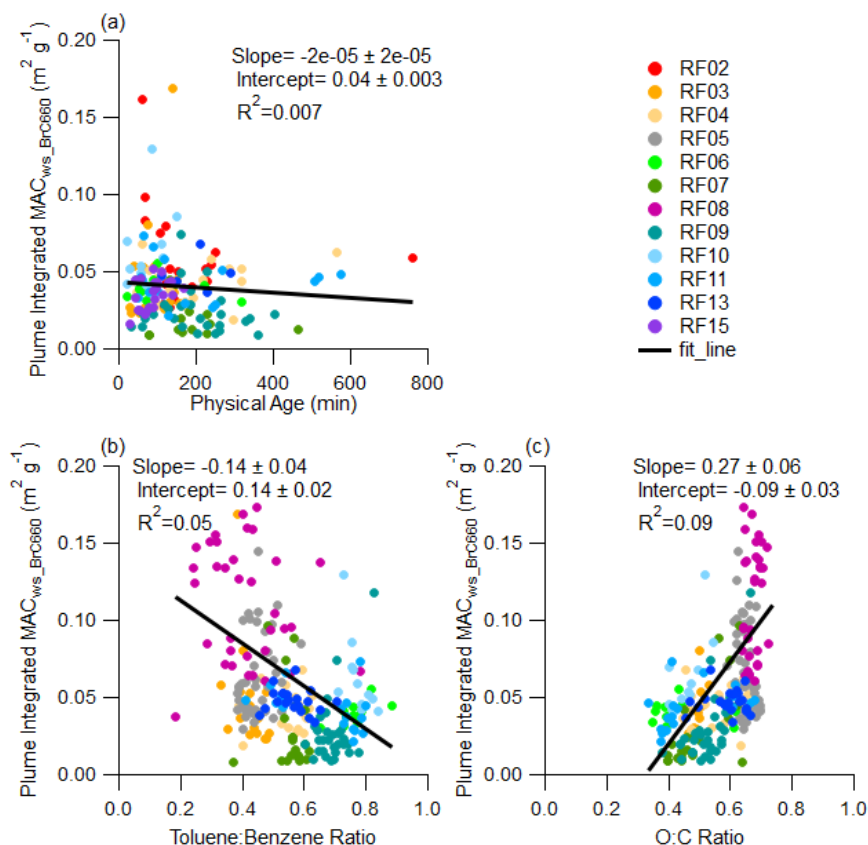


Figure 11: Plume integrated MAC_{ws_BrC660} variations with (a) Physical Age; (b) toluene:benzene ratio and (c) O:C ratio. RF05 and RF08 were measuring mixed aged smokes, during which the fire source cannot be identified, and therefore the physical age is unavailable for both flights.

520 The total MAC of BrC and lensing at 660 (measured by PAS, $MAC_{BrC+lensing_660}$) is also compared with
 521 markers of chemical age (Fig. 12). $MAC_{BrC+lensing_660}$ includes lensing, water-soluble BrC, and water-insoluble BrC.
 522 $MAC_{BrC+lensing_660}$ also shows an increasing trend with chemical oxidation, which is consistent with the trend in
 523 MAC_{ws_BrC660} . Again, it is important to point out that while there is a weak trend for some individual flights, much of
 524 the trend of increasing MAC at 660 nm results from combining data from all the fires and much of the trend may be
 525 caused by emissions from different fires having different properties. Despite this, it is clear that plumes that appear
 526 chemically older by either the toluene:benzene ratio or the O:C ratio actually have larger MAC's in the red wavelength
 527 than plumes that appear chemically younger, a result that is exactly the opposite of the bleaching of BrC often seen at
 528 shorter wavelengths. In addition, these chemically "older" plumes have less BC, OA, and WSOC along with smaller
 529 bulk absorption. That is to say, when chemical markers indicate an "old" plume, the fire tends to emit darker (Fig. 11
 530 and Fig. 12) organic aerosol, but less of it (Fig. 5 g-h and Fig. 6) resulting in less bulk absorption (Fig. 5c and 5f). The
 531 mean value of $MAC_{BrC+lensing_660}$ is $0.11 m^2 g^{-1}$ (with a standard deviation of 0.06), which is larger than the 0.06 average



532 of MAC_{ws_BrC660} , a result we have attributed to the lensing effect, but which could also partially be the result of water-
533 insoluble BrC having a higher MAC than water-soluble BrC.

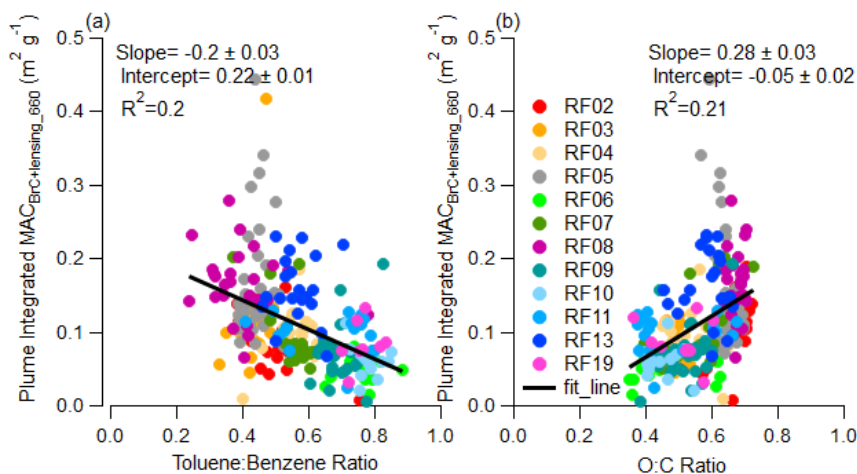


Figure 12: Plume integrated $MAC_{BrC+lensing_660}$ variations with (a) toluene:benzene ratio and (b) O:C ratio.

534 The ratio of BC:OA has been shown to correlate to the optical properties of biomass burning aerosol (Pokhrel
535 et al, 2016; Saleh et al., 2014). During WE-CAN, $MAC_{BrC+lensing_660}$ showed an increasing trend with increasing
536 BC:OA ratio (Fig. S6), which is similar to Saleh et al. (2014), who found that the imaginary part of the refractive
537 index of OA at 550 nm increases with the BC:OA ratio. This consistency suggests that MAC of BrC at 550 nm and
538 660 nm have the same behavior in that BrC grows more absorbing as the BC:OA ratio increases.

539 3.2 Characteristics of BrC at 405 nm

540 3.2.1 Behavior of $MAC_{BrC+lensing_405}$

541 Palm et al. (2020) utilized data from both WE-CAN and Monoterpene and Oxygenated aromatic Oxidation
542 at Night and under LIGHTs (MOONLIGHT) campaigns and found that evaporated biomass-burning POA is the
543 dominant source of the biomass-burning SOA in wildfire plumes, which happened in the first a few hours after
544 emission. They also found that for those SOA that formed from oxidation, phenolic compounds contribute $29 \pm 15\%$
545 of BrC absorption at 405 nm. In this section, characteristics of BrC were also analyzed at 405 nm to understand if the
546 behavior was similar or different to BrC decay at 660 nm. BrC at 405 nm was calculated in the same way that it was
547 calculated at 660 nm, following Eq. 3, and therefore it also has a contribution from the lensing effect. Figure 13 shows
548 the plume integrated $MAC_{BrC+lensing_405}$ variations with (a) Physical Age and (b) MCE. Similar to 660 nm,
549 $MAC_{BrC+lensing_405}$ varies from fire to fire and no clear trend can be found with increasing physical age or MCE. Similar
550 behavior was also observed in Western wildfires at 405 nm in FIREX-AQ (Zeng et al., 2022). The $MAC_{BrC+lensing_405}$,
551 varies from $0.08 \text{ m}^2 \text{ g}^{-1}$ to $1.6 \text{ m}^2 \text{ g}^{-1}$ with a mean value of $0.59 \text{ m}^2 \text{ g}^{-1}$ and a standard deviation of 0.19. The largest
552 values are from RF05, the flight through California, Oregon, and Idaho, where aged smoke from different fires was
553 mixed. The large $MAC_{BrC+lensing_405}$ in RF05 is related to relatively small OA (Fig. 5 g-h), which occurred when the



554 plane left the smoke-filled boundary layer during RF05. If we exclude $MAC_{BrC+lensing_405}$ from RF05, the values range
 555 from $0.08 \text{ m}^2 \text{ g}^{-1}$ to $1.09 \text{ m}^2 \text{ g}^{-1}$, but still have a mean value of $0.59 \text{ m}^2 \text{ g}^{-1}$ and a standard deviation of 0.15. Again, we
 556 note that this value includes the contribution of lensing. Despite this, our results lie in the same range as those measured
 557 without the contribution of lensing of $0.31 \pm 0.09 \text{ m}^2 \text{ g}^{-1}$ measured in CLARIFY-2017 (Taylor, 2020), $0.13\text{-}2.0 \text{ m}^2 \text{ g}^{-1}$
 558 ¹ measured in FIREX-AQ (Zeng et al., 2022), and $0.25\text{-}1.18 \text{ m}^2 \text{ g}^{-1}$ measured in ORACLES (Zhang et al., 2022).

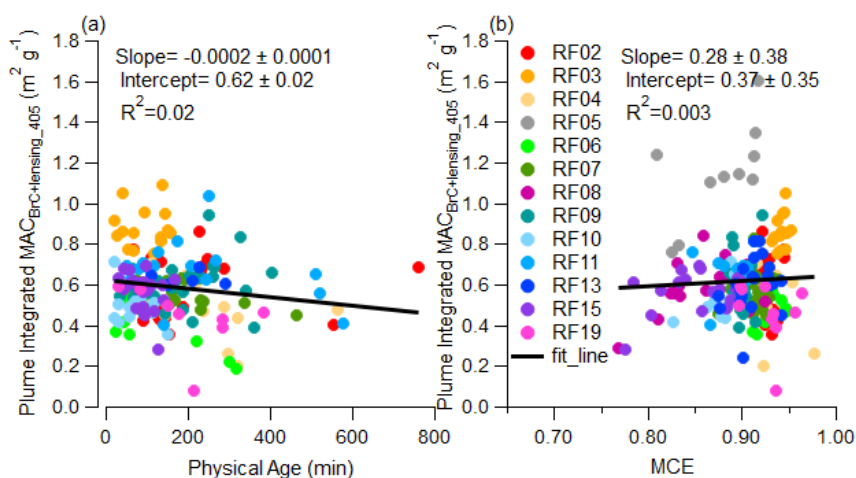


Figure 13: Plume integrated $MAC_{BrC+lensing_405}$ variations with (a) Physical Age and (b) MCE

559 Figure 14 shows the behavior of brown carbon at 405 nm with markers of chemical aging. Very weak or non-
 560 trends are observed. If there is any trend, it is a slight increase in $MAC_{BrC+lensing_405}$ with decreasing toluene:benzene
 561 ratio, which is consistent with the results for $MAC_{BrC+lensing_660}$ (Fig. 12) and MAC_{ws_BrC660} (Fig. 11). The flat or slightly
 562 increasing trend with increasing oxidation shows that the decrease in total aerosol absorption with markers of chemical
 563 age is due to a decrease in OA (Fig. 5 g-h) because the BrC is actually darker in oxidized plumes at all wavelengths.
 564 It is important to remember that most of the trends observed in WE-CAN are caused by emissions from different fires
 565 versus variations within a fire, which tend to be quite small. Consistent results for the behavior of MAC_{BrC} at different
 566 wavelengths derived using different instruments (PAS and PILS) is further evidence that BrC decay does not occur in
 567 the WE-CAN dataset, or at least that plume integrated results cannot capture the BrC decay that might be occurring
 568 at the edges of the plume. While further research focused on the edge of the plumes, which often appear highly
 569 oxidized, is needed, this is beyond the scope of the current work. Despite this, it is the plume integrated results that
 570 are relevant for climate impacts and for comparison to model output, discussed in the following section.

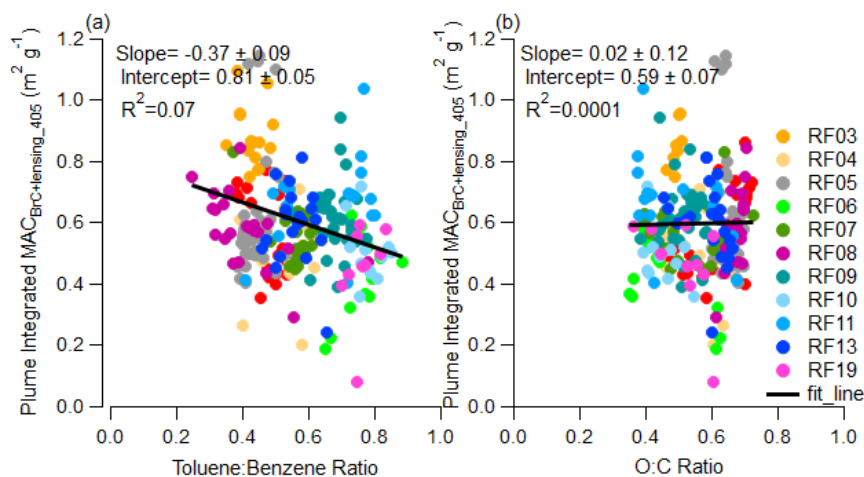


Figure 14: Plume integrated $MAC_{BrC+lensing_405}$ variations with (a) toluene:benzene ratio and (b) O:C ratio

571 RF05 and RF08 are presented as case studies again to investigate the behavior of $MAC_{BrC+lensing_405}$ in mixed
 572 plumes emitted from different fire sources. Figure 15 is similar to Fig. 8, but with $MAC_{BrC+lensing_405}$ instead of
 573 MAC_{BrC660} . For the case of RF05 (Fig. 15a) $MAC_{BrC+lensing_405}$ varied from $0.36 \text{ m}^2 \text{ g}^{-1}$ to $1.52 \text{ m}^2 \text{ g}^{-1}$ with an average
 574 of $0.66 \text{ m}^2 \text{ g}^{-1}$ and a standard deviation of $0.26 \text{ m}^2 \text{ g}^{-1}$, the SSA_{450} averaged 0.94 with a standard deviation of 0.02,
 575 which is similar to SSA_{660} . The $MAC_{BrC+lensing_405}$ is larger when CO mixing ratio is higher, but does not have a
 576 significant correlation with any other variables shown in Fig. 15. For the case of RF08 (Fig. 15b) $MAC_{BrC+lensing_405}$ is
 577 more stable than in RF05, and varied from $0.25 \text{ m}^2 \text{ g}^{-1}$ to $0.88 \text{ m}^2 \text{ g}^{-1}$ with an average of $0.59 \text{ m}^2 \text{ g}^{-1}$ and a standard
 578 deviation of $0.14 \text{ m}^2 \text{ g}^{-1}$, the SSA_{450} average was 0.95 with a standard deviation of 0.01. The regional integrated
 579 $MAC_{BrC+lensing_405}$ is even more stable with an average value of $0.59 \text{ m}^2 \text{ g}^{-1}$ and a standard deviation of $0.07 \text{ m}^2 \text{ g}^{-1}$.

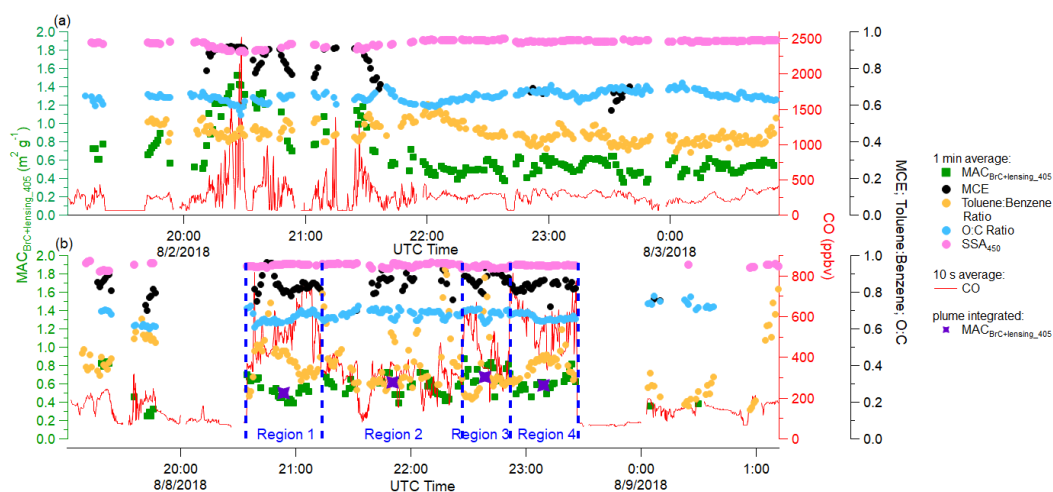


Figure 15: Time series of plume properties during (a) RF05, and (b) RF08(Central Valley of California). Different square and round markers indicate 1 min averages of different variables as shown in the legend, and the red solid line represents 10 s averages of the mixing ratio of CO. Purple stars in RF08 indicate region integrated $MAC_{BrC+lensing_405}$ (individual regions are separated based on the concentration of CO, and indicated by blue dashed lines).

580 When comparing $MAC_{BrC+lensing_405}$ with altitude and temperature (Fig. 16), it has the same behavior with
 581 MAC_{BC660} in that $MAC_{BrC+lensing_405}$ stays relatively constant with both altitude and temperature. In addition, when
 582 $MAC_{BrC+lensing_405}$ is plotted vs. ΔCO (not shown), no clear change in $MAC_{BrC+lensing_405}$ is seen due to dilution.
 583 Therefore, both $MAC_{BrC+lensing_405}$ and MAC_{BC660} do not appear to be affected by altitude or temperature during WE-
 584 CAN.

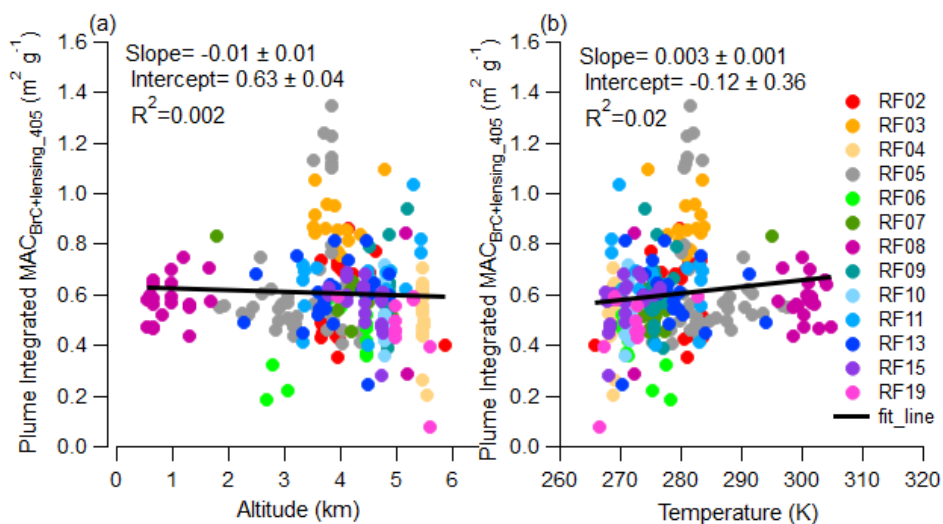


Figure 16: Plume integrated $MAC_{BrC+lensing_405}$ variations with (a) Altitude and (b) Temperature



585 When comparing the relationship between $MAC_{BrC+lensing_405}$ with the BC:OA ratio (Fig. S7), there is not a
586 clear increasing trend, and the correlation is worse than that at 660 nm (Fig. S6). However, the increasing trend still
587 exists in most individual flights (not in RF04 and RF10). The increasing trend is not as clear as in Saleh et al. (2014),
588 most probably because the range of BC:OA ratios observed during WE-CAN (0.007~0.061) is much smaller than that
589 (0.005~0.7) observed in Saleh's work. Even in their work, the increasing trend is not very clear if one only focuses on
590 the region where the BC:OA ratio is less than 0.03. Also, the Saleh et al. results were obtained from laboratory burns
591 and not wildfires, which might also cause a discrepancy.

592 **3.2.2 Comparison of WE-CAN Results to Modeling Studies**

593 The BC:OA ratios measured during WE-CAN were utilized in the Saleh et al. parameterization (2014), which
594 provides an imaginary part for the refractive index of BrC ($k_{BrC,\lambda}$) as a function of the BC:OA ratio. The mean BC:OA
595 ratio for each plume was used in the parameterization, which gave an average k_{BrC} of 0.025, 0.013, 0.009, respectively,
596 at 405 nm, 550 nm and 660nm. Mie theory was then used to calculate the MAC for BrC, in which we assumed a real
597 part of the refractive index of 1.7 for BrC (same as Saleh et al., 2014), a volume mean diameter measured for each
598 plume, and a density of 1.4 g cm^{-3} . Figure 17 compares the observed $MAC_{BrC+lensing}$ and MAC_{ws_BrC} with the value
599 calculated from the Saleh parameterization with inputs from WE-CAN. In both the observations and the
600 parameterization, the MAC_{BrC} decreases as wavelength increases. However, the Saleh parameterization is always
601 significantly larger than the observations. The MAC_{BrC} from the Saleh parameterization, which does not include
602 lensing effects, is a factor of 3.4 and 2.8 larger than the observed $MAC_{BrC+lensing}$ at 405 nm and 660 nm, respectively.
603 The range of BC:OA ratios during WE-CAN (0.007~0.061) is much smaller than that (0.005~0.7) used in Saleh's
604 work, and the parameterization failed to capture absorbing aerosol properties for this study. The discrepancy could be
605 partly because the data Saleh et al. used for their parameterization comes from controlled laboratory burns and not
606 wildfires, or because of the sensitivity of MAC_{BrC} to density when using the Saleh parameterization. When we increase
607 particle density from 1.4 g cm^{-3} to 1.7 g cm^{-3} , the Saleh parameterization median MAC_{BrC} decreases to $1.6 \text{ m}^2 \text{ g}^{-1}$ and
608 $0.24 \text{ m}^2 \text{ g}^{-1}$, respectively, at 405 nm and 660 nm (a factor of 2.8 and 2.3, respectively, compared to observed MAC_{BrC}
609 at 405 nm and 660 nm). This suggests that the Saleh parameterization overestimates the absorption property of biomass
610 aerosol especially for fresh emitted aerosols and more parameterizations need to be developed. Carter et al. (2021)
611 utilized the Saleh parameterization for BrC absorption in the GEOS-Chem model and also found that the Saleh model
612 overestimated BrC absorption for WE-CAN. It was hypothesized that the overestimation was due to the lack of a
613 bleaching process for BrC in the model and offset part of the overestimation by bringing in bleaching into the model.
614 However, our results show that the overestimation in the model is caused by an incorrect refractive index.

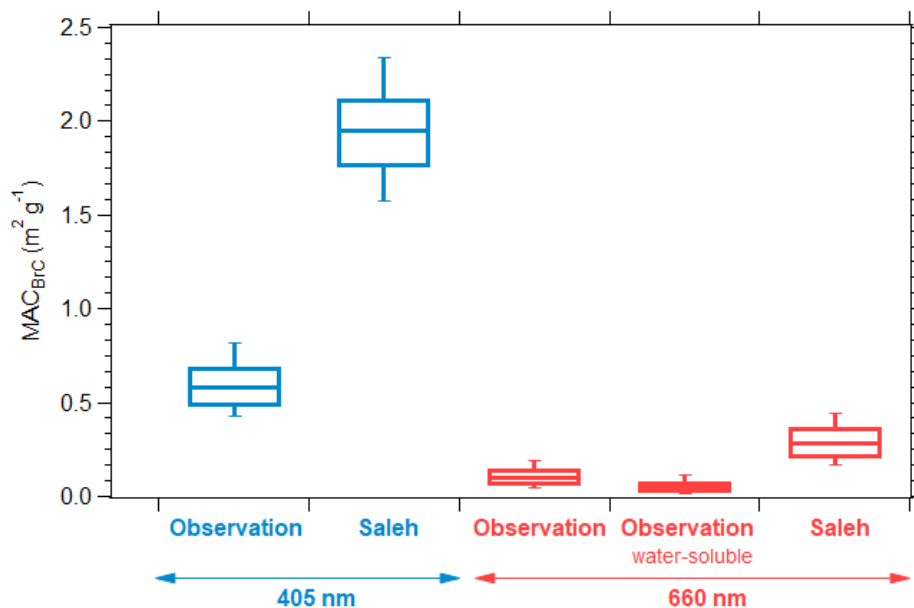


Figure 17: Boxplot summary for observed and parameterized (Saleh) MAC_{BrC} at 405 nm (blue) and 660 nm (red). On each box the central line represents the median, the top and bottom edge represents 75% and 25%, the top and bottom whisker represents 90% and 10%.

615 4 Conclusion

616 In this study, we presented results that help us better understand the ability of wildfire aerosol emissions to
617 absorb visible light and how those properties change after emission. We presented mass absorption coefficients (MAC)
618 for black and brown carbon from Western United States wildfires measured during the WE-CAN campaign at both
619 short and long visible wavelengths (MAC_{BC660}, MAC_{BrC+lensing_660}, MAC_{ws_BrC660}, MAC_{BrC+lensing_405}). We also
620 investigated single scattering albedo (SSA), total scattering and total absorption at 660. We observed that the mass
621 absorption coefficient of black carbon stayed relatively constant across all plumes measured and at all physical ages
622 (ages up to 15 hours observed), with an averaged MAC_{BC660} of 10.9 ± 2.1 m² g⁻¹ (average ± standard deviation). This
623 average showed no variation with altitude or temperature, and we saw no evidence that MAC_{BC660} is correlated to
624 MCE. Even in highly aged plumes with emissions mixed from multiple fires (RF05 and RF08), the MAC_{BC660} is
625 similar in magnitude and consistency with an average of 11.3 ± 1.8 m² g⁻¹. Both the fact that this MAC is significantly
626 larger than the MAC for uncoated BC (often cited to be ~ 6.3 m² g⁻¹) and the fact that the MAC remains relatively
627 constant across different fires and different plume ages are key insights that can improve models of aerosol optical
628 properties in wildfire emissions.

629 We find that total organic aerosol (OA) and water-soluble organic carbon (WSOC) are strongly correlated
630 with markers of chemical age. OA and WSOC (both normalized to CO) decrease with decreasing toluene:benzene
631 ratio or increasing O:C ratio. However, this phenomenon is observed in variations between different fire sources rather



632 than during the aging of individual fire plumes. We interpret this variability to mean the fires either had different
633 emission ratios of toluene:benzene and O:C or the smoke underwent rapid secondary chemistry prior to the first plume
634 pass in WE-CAN. Regardless, the correlations are relatively strong (R^2 of 0.24 to 0.71) and provide a potential link
635 between chemical markers and total organic aerosol amounts across a wide range of fires. While OA and WSOC
636 decrease with decreasing toluene:benzene or increasing O:A, MAC_{BC660} actually shows a weak increasing trend with
637 these same markers of aging, showing that while the total amount of organic aerosol is decreasing, the ability of the
638 organic to absorb per mass is staying relatively constant, or even increasing.

639 Through a novel use of PILS data, we find that BrC contributes 41-80% of non-BC absorption at 660 nm
640 (assuming $6.3 \text{ m}^2 \text{ g}^{-1}$ as the MAC of BC core at 660 nm). BrC contributes, on average, 26% of total absorption, but
641 the absorption cross section of water-soluble BrC is relatively small at 660 nm, with a MAC_{ws_BrC660} of $0.06 \pm 0.04 \text{ m}^2$
642 g^{-1} , which does not change with physical age. The average $MAC_{BrC+lensing_660}$ derived from the PAS (which includes
643 both brown carbon absorption and lensing of black carbon) is $0.11 \pm 0.06 \text{ m}^2 \text{ g}^{-1}$.

644 In the blue visible wavelengths where brown carbon is more often thought about, $MAC_{BrC+lensing_405}$ is $0.59 \pm$
645 $0.19 \text{ m}^2 \text{ g}^{-1}$ and shows little variation with physical age or MCE. There are weak increasing trends in all the MAC_{BrC}
646 data we obtained (MAC_{ws_BrC660} , $MAC_{BrC+lensing_660}$ and $MAC_{BrC+lensing_405}$) with markers of chemical age
647 (toluene:benzene, O:C), while bulk absorption of total aerosol decreases with these same markers of chemical age. In
648 highly aged plumes from multiple fires (RF05 and RF08), the $MAC_{BrC+lensing_405}$ has an average value of $0.63 \pm 0.2 \text{ m}^2$
649 g^{-1} , suggesting that brown carbon remains significantly absorbing even at relatively longer ages.

650 Utilizing a common parameterization for BrC refractive index from Saleh et al. (2014), with measured inputs
651 for the BC:OA ratio and particle size, we calculated the theoretical MAC_{BrC660} and MAC_{BrC405} , and they were 2.3~3.4
652 times larger than the measured $MAC_{BrC+lensing}$ during WE-CAN. While this discrepancy has been resolved previously
653 by implementing bleaching into model schemes, we show that this is probably the incorrect explanation given the
654 MAC of brown carbon is actually higher when markers (O:C, toluene:benzene) suggest more oxidation. We suggest
655 a new BrC parameterization is needed to represent wildfire optical properties in the Western United States. We also
656 note that there needs to be better terminology to distinguish between decreasing absorption caused by losses of organic
657 aerosol mass versus decreasing absorption caused by changes in the mass absorption cross section (MAC) of the
658 aerosol. Finally, these results are based on the plume integration method, which might neglect aerosol decay at the
659 edge of the plume where oxidation and evaporation are more rapid compared to the center of the plume. While this
660 effect may be important for studying mechanisms of smoke evolution, it does not affect mean properties, which are
661 what ultimately affect climate and are comparable to modeling results.

662 Data Availability

663 The WE-CAN data can be found at http://data.eol.ucar.edu/master_lists/generated/we-can/.

664 The DOI for each data set used in this work are:

665 PAS and CAPS PM_{SSA} : <https://doi.org/10.26023/K8P0-X4T3-TN06>

666 PILS1: <https://doi.org/10.26023/9H07-MD9K-430D> and <https://doi.org/10.26023/CRHY-NDT9-C30V>

667 PILS2: <https://doi.org/10.26023/7TAN-TZMD-680Y>



668 SP2: <https://doi.org/10.26023/P8R2-RAB6-N814>
669 UHSAS: <https://doi.org/10.26023/BZ4F-EAC4-290W>
670 PTR-ToF-MS: <https://doi.org/10.26023/K9F4-2CNH-EQ0W>
671 HR-AMS: <https://doi.org/10.26023/MM2Y-ZGFQ-RB0B>
672 Picarro: <https://doi.org/10.26023/NNYM-Z18J-PX0Q>
673 miniQCL: <https://doi.org/10.26023/Q888-WZRD-B70F>

674 **Author Contributions**

675 SMM designed the project. YS wrote the paper. YS, RPP, APS, EJTL, LAG, DKF, WP, LH, DWT, TC, EVF, and
676 SMM collected and analyzed data.

677 **Competing Interests**

678 The authors declare that they have no conflict of interest.

679 **Acknowledgements**

680 The 2018 WE-CAN field campaign was supported by the U.S. National Science Foundation through grants AGS-
681 1650493 (U of Wyoming), AGS-1650786 (Colorado State U), AGS-1650275 (U of Montana), AGS-1650288 (U of
682 Colorado at Boulder), and the National Oceanic and Atmospheric Administration (Award # NA17OAR4310010,
683 Colorado State U). This material is based upon study supported by the National Center for Atmospheric Research,
684 which is a major facility sponsored by the National Science Foundation under Cooperative Agreement no. 1852977.

685

686 The authors acknowledge support from AGS-1650493 for YS, SMM and RPP, AGS-1650786 for APS and EJTL,
687 AGS-2144896 for LH and WP, AGS-1650288 for DWT, NOAA Climate Program Office's Atmospheric Chemistry,
688 Carbon Cycle, and Climate program (Grant NA17OAR4310010) for DKF and LAG.

689 **References**

690 Aiken, A. C., Decarlo, P. F., Kroll, J. H., Worsnop, D. R., Huffman, J. A., Docherty, K. S., et al. (2008). O/C and
691 OM/OC ratios of primary, secondary, and ambient organic aerosols with high-resolution time-of-flight aerosol
692 mass spectrometry. *Environmental Science and Technology*, 42(12), 4478–4485.
693 <https://doi.org/10.1021/es703009q>
694 Akagi, S. K., Yokelson, R. J., Wiedinmyer, C., Alvarado, M. J., Reid, J. S., Karl, T., et al. (2011). Emission factors
695 for open and domestic biomass burning for use in atmospheric models. *Atmospheric Chemistry and Physics*,
696 11(9), 4039–4072. <https://doi.org/10.5194/acp-11-4039-2011>



- 697 Andreae, M. O. (2019). Emission of trace gases and aerosols from biomass burning – An updated assessment.
698 *Atmospheric Chemistry and Physics Discussions*, 1–27. <https://doi.org/10.5194/acp-2019-303>
- 699 Andreae, M. O., & Gelencsér, A. (2006). Black carbon or brown carbon? The nature of light-absorbing carbonaceous
700 aerosols. *Atmospheric Chemistry and Physics*, 6, 3131–3148. <https://doi.org/10.5194/acp-6-3131-2006>
- 701 Bahadur, R., Praveen, P. S., Xu, Y., & Ramanathan, V. (2012). Solar absorption by elemental and brown carbon
702 determined from spectral observations. *Proceedings of the National Academy of Sciences*, 109(43), 17366–
703 17371. <https://doi.org/10.1073/pnas.1205910109>
- 704 Bohren, C. F., and Huffman, D. R. (1983). Absorption and Scattering of Light by Small Particles. John Wiley & Sons,
705 Inc.
- 706 Bond, T. C., & Bergstrom, R. W. (2006). Light absorption by carbonaceous particles: An investigative review. *Aerosol*
707 *Science and Technology*, 40(1), 27–67. <https://doi.org/10.1080/02786820500421521>
- 708 Bond, T. C., Habib, G., & Bergstrom, R. W. (2006). Limitations in the enhancement of visible light absorption due to
709 mixing state. *Journal of Geophysical Research Atmospheres*, 111(20), 1–13.
710 <https://doi.org/10.1029/2006JD007315>
- 711 Bond, T. C., Doherty, S. J., Fahey, D. W., Forster, P. M., Berntsen, T., Deangelo, B. J., et al. (2013). Bounding the
712 role of black carbon in the climate system: A scientific assessment. *Journal of Geophysical Research*
713 *Atmospheres*, 118(11), 5380–5552. <https://doi.org/10.1002/jgrd.50171>
- 714 Brown, H., Liu, X., Pokhrel, R., Murphy, S., Lu, Z., Saleh, R., et al. (2021). Biomass burning aerosols in most climate
715 models are too absorbing. *Nature Communications*, 12(1), 1–15. <https://doi.org/10.1038/s41467-020-20482-9>
- 716 Burke, M., Driscoll, A., Heft-Neal, S., Xue, J., Burney, J., & Wara, M. (2021). The changing risk and burden of
717 wildfire in the United States. *Proceedings of the National Academy of Sciences of the United States of America*,
718 118(2), 1–6. <https://doi.org/10.1073/PNAS.2011048118>
- 719 Canagaratna, M. R., Jimenez, J. L., Kroll, J. H., Chen, Q., Kessler, S. H., Massoli, P., et al. (2015). Elemental ratio
720 measurements of organic compounds using aerosol mass spectrometry : characterization , improved calibration ,
721 and implications. *Atmospheric Chemistry and Physics*, 15(1), 253–272. [https://doi.org/10.5194/acp-15-253-](https://doi.org/10.5194/acp-15-253-2015)
722 [2015](https://doi.org/10.5194/acp-15-253-2015)
- 723 Cappa, C. D., Onasch, T. B., Massoli, P., Worsnop, D. R., Bates, T. S., Cross, E. S., et al. (2012). Radiative absorption
724 enhancements due to the mixing state of atmospheric black carbon. *Science*, 337(6098), 1078–1081.
725 <https://doi.org/10.1126/science.1223447>
- 726 Cappa, C. D., Zhang, X., Russell, L. M., Collier, S., Lee, A. K. Y., Chen, C. L., et al. (2019). Light Absorption by
727 Ambient Black and Brown Carbon and its Dependence on Black Carbon Coating State for Two California, USA,
728 Cities in Winter and Summer. *Journal of Geophysical Research: Atmospheres*, 124(3), 1550–1577.
729 <https://doi.org/10.1029/2018JD029501>
- 730 Carter, T. S., Heald, C. L., Cappa, C. D., Kroll, J. H., Campos, T. L., Coe, H., et al. (2021). Investigating Carbonaceous
731 Aerosol and its Absorption Properties from Fires in the western US (WE-CAN) and southern Africa (ORACLES
732 and CLARIFY). *Journal of Geophysical Research Atmospheres*, 1–28. <https://doi.org/10.1029/2021JD034984>



- 733 Chen, M., Sun, Z., Davis, J. M., Liu, Y. A., Corr, C. A., & Gao, W. (2019). Improving the mean and uncertainty of
734 ultraviolet multi-filter rotating shadowband radiometer in situ calibration factors: Utilizing Gaussian process
735 regression with a new method to estimate dynamic input uncertainty. *Atmospheric Measurement Techniques*,
736 *12*(2), 935–953. <https://doi.org/10.5194/amt-12-935-2019>
- 737 Cho, C., Kim, S. W., Lee, M., Lim, S., Fang, W., Gustafsson, Ö., et al. (2019). Observation-based estimates of the
738 mass absorption cross-section of black and brown carbon and their contribution to aerosol light absorption in
739 East Asia. *Atmospheric Environment*, *212*(November 2018), 65–74.
740 <https://doi.org/10.1016/j.atmosenv.2019.05.024>
- 741 Chylek, P., Lee, J. E., Romonosky, D. E., Gallo, F., Lou, S., Shrivastava, M., et al. (2019). Mie Scattering Captures
742 Observed Optical Properties of Ambient Biomass Burning Plumes Assuming Uniform Black, Brown, and
743 Organic Carbon Mixtures. *Journal of Geophysical Research: Atmospheres*, *124*(21), 11406–11427.
744 <https://doi.org/10.1029/2019JD031224>
- 745 Craig, L., Moharreri, A., Schanot, A., Rogers, D. C., Dhaniyala, S., Craig, L., et al. (2013a). Characterizations of
746 Cloud Droplet Shatter Artifacts in Two Airborne Aerosol Inlets. *Aerosol Science and Technology*, *47*:6, 662–
747 671. <https://doi.org/10.1080/02786826.2013.780648>
- 748 Craig, L., Schanot, A., Moharreri, A., Rogers, D. C., & Dhaniyala, S. (2013b). Design and Sampling Characteristics
749 of a New Airborne Aerosol Inlet for Aerosol Measurements in Clouds. *Journal of Atmospheric and Oceanic*
750 *Technology*, *30*, 1123–1135. <https://doi.org/10.1175/JTECH-D-12-00168.1>
- 751 Craig, L., Moharreri, A., Rogers, D. C., Anderson, B., & Dhaniyala, S. (2014). Aircraft-Based Aerosol Sampling in
752 Clouds : Performance Characterization of Flow-Restriction Aerosol Inlets. *Journal of Atmospheric and Oceanic*
753 *Technology*, *31*, 2512–2521. <https://doi.org/10.1175/JTECH-D-14-00022.1>
- 754 Duarte, R. M. B. O., Freire, S. M. S. C., & Duarte, A. C. (2015). Investigating the water-soluble organic functionality
755 of urban aerosols using two-dimensional correlation of solid-state ¹³C NMR and FTIR spectral data.
756 *Atmospheric Environment*, *116*, 245–252. <https://doi.org/10.1016/j.atmosenv.2015.06.043>
- 757 Duarte, R. M. B. O., Piñeiro-Iglesias, M., López-Mahía, P., Muniategui-Lorenzo, S., Moreda-Piñeiro, J., Silva, A. M.
758 S., & Duarte, A. C. (2019). Comparative study of atmospheric water-soluble organic aerosols composition in
759 contrasting suburban environments in the Iberian Peninsula Coast. *Science of the Total Environment*, *648*, 430–
760 441. <https://doi.org/10.1016/j.scitotenv.2018.08.171>
- 761 Eatough, D. J., Wadsworth, A., Eatough, D. A., Crawford, J. W., Hansen, L. D., & Lewis, E. A. (1993). A multiple-
762 system, multi-channel diffusion denuder sampler for the determination of fine-particulate organic material in
763 the atmosphere. *Atmospheric Environment Part A, General Topics*, *27*(8), 1213–1219.
764 [https://doi.org/10.1016/0960-1686\(93\)90247-V](https://doi.org/10.1016/0960-1686(93)90247-V)
- 765 Finessi, E., Decesari, S., Paglione, M., Giulianelli, L., Carbone, C., Gilardoni, S., et al. (2012). Determination of the
766 biogenic secondary organic aerosol fraction in the boreal forest by NMR spectroscopy. *Atmospheric Chemistry*
767 *and Physics*, *12*(2), 941–959. <https://doi.org/10.5194/acp-12-941-2012>



- 768 Ford, B., Val Martin, M., Zelasky, S. E., Fischer, E. V., Anenberg, S. C., Heald, C. L., & Pierce, J. R. (2018). Future
769 Fire Impacts on Smoke Concentrations, Visibility, and Health in the Contiguous United States. *GeoHealth*, 2(8),
770 229–247. <https://doi.org/10.1029/2018gh000144>
- 771 Foster, K., Pokhrel, R., Burkhart, M., & Murphy, S. (2019). A novel approach to calibrating a photoacoustic absorption
772 spectrometer using polydisperse absorbing aerosol. *Atmospheric Measurement Techniques*, 12(6), 3351–3363.
773 <https://doi.org/10.5194/amt-12-3351-2019>
- 774 Fuller, K. A., & Kreidenweis, S. M. (1999). Effects of mixing on extinction by carbonaceous particles. *Journal of*
775 *Geophysical Research*, 104(D13), 15941–15954. <https://doi.org/10.1029/1998JD100069>
- 776 Garofalo, L. A., Pothier, M. A., Levin, E. J. T., Campos, T., Kreidenweis, S. M., & Farmer, D. K. (2019). Emission
777 and Evolution of Submicron Organic Aerosol in Smoke from Wildfires in the Western United States. *ACS Earth*
778 *and Space Chemistry*, 3(7), 1237–1247. <https://doi.org/10.1021/acsearthspacechem.9b00125>
- 779 Grieshop, A. P., Logue, J. M., Donahue, N. M., & Robinson, A. L. (2009). Laboratory investigation of photochemical
780 oxidation of organic aerosol from wood fires 1: Measurement and simulation of organic aerosol evolution.
781 *Atmospheric Chemistry and Physics*, 9(4), 1263–1277. <https://doi.org/10.5194/acp-9-1263-2009>
- 782 Gouw, J. A. De, Middlebrook, A. M., Warneke, C., Goldan, P. D., Kuster, W. C., Roberts, J. M., et al. (2005). Budget
783 of organic carbon in a polluted atmosphere : Results from the New England Air Quality Study in 2002. *Journal*
784 *of Geophysical Research*, 110, 1–22. <https://doi.org/10.1029/2004JD005623>
- 785 Healy, R. M., Wang, J. M., Jeong, C. H., Lee, A. K. Y., Willis, M. D., Jaroudi, E., et al. (2015). Light-absorbing
786 properties of ambient black carbon and brown carbon from fossil fuel and biomass burning sources. *Journal of*
787 *Geophysical Research: Atmospheres*, 120(13), 6619–6633. <https://doi.org/10.1002/2015JD023382>
- 788 Hecobian, A., Zhang, X., Zheng, M., Frank, N., Edgerton, E. S., & Weber, R. J. (2010). Water-soluble organic aerosol
789 material and the light-absorption characteristics of aqueous extracts measured over the Southeastern United
790 States. *Atmospheric Chemistry and Physics*, 10(13), 5965–5977. <https://doi.org/10.5194/acp-10-5965-2010>
- 791 Hurteau, M. D., Westerling, A. L., Wiedinmyer, C., & Bryant, B. P. (2014). Projected effects of climate and
792 development on California wildfire emissions through 2100. *Environmental Science and Technology*, 48(4),
793 2298–2304. <https://doi.org/10.1021/es4050133>
- 794 Kirchstetter, T. W., Novakov, T., & Hobbs, P. V. (2004). Evidence that the spectral dependence of light absorption
795 by aerosols is affected by organic carbon. *Journal of Geophysical Research D: Atmospheres*, 109(21), 1–12.
796 <https://doi.org/10.1029/2004JD004999>
- 797 Krasowsky, T. S., McMeeking, G. R., Wang, D., Sioutas, C., & Ban-Weiss, G. A. (2016). Measurements of the impact
798 of atmospheric aging on physical and optical properties of ambient black carbon particles in Los Angeles.
799 *Atmospheric Environment*, 142, 496–504. <https://doi.org/10.1016/j.atmosenv.2016.08.010>
- 800 Kleinman, L. I., Sedlacek, A. J., Adachi, K., Buseck, P. R., Collier, S., Dubey, M. K., et al. (2020). Rapid evolution
801 of aerosol particles and their optical properties downwind of wildfires in the western US. *Atmospheric Chemistry*
802 *and Physics*, 20(21), 13319–13341. <https://doi.org/10.5194/acp-20-13319-2020>



- 803 Lack, D. A., Lovejoy, E. R., Baynard, T., Pettersson, A., & Ravishankara, A. R. (2006). Aerosol Absorption
804 Measurement using Photoacoustic Spectroscopy: Sensitivity, Calibration, and Uncertainty Developments.
805 *Aerosol Science and Technology*, 40(9), 697–708. <https://doi.org/10.1080/02786820600803917>
- 806 Lack, D. A., & Cappa, C. D. (2010). Impact of brown and clear carbon on light absorption enhancement, single scatter
807 albedo and absorption wavelength dependence of black carbon. *Atmospheric Chemistry and Physics*, 10(9),
808 4207–4220. <https://doi.org/10.5194/acp-10-4207-2010>
- 809 Lack, D. A., Langridge, J. M., Bahreini, R., Cappa, C. D., Middlebrook, A. M., & Schwarz, J. P. (2012a). Brown
810 carbon and internal mixing in biomass burning particles. *Proceedings of the National Academy of Sciences of
811 the United States of America*, 109(37), 14802–14807. <https://doi.org/10.1073/pnas.1206575109>
- 812 Lack, D. A., Richardson, M. S., Law, D., Langridge, J. M., Cappa, C. D., McLaughlin, R. J., & Murphy, D. M. (2012b).
813 Aircraft Instrument for Comprehensive Characterization of Aerosol Optical Properties, Part 2: Black and Brown
814 Carbon Absorption and Absorption Enhancement Measured with Photo Acoustic Spectroscopy. *Aerosol Science
815 and Technology*, 46(5), 555–568. <https://doi.org/10.1080/02786826.2011.645955>
- 816 Lindaas, J., Pollack, I. B., Garofalo, L. A., Pothier, M. A., Farmer, D. K., Kreidenweis, S. M., et al. (2021). Emissions
817 of Reactive Nitrogen From Western U.S. Wildfires During Summer 2018. *Journal of Geophysical Research:
818 Atmospheres*, 126(2), 1–21. <https://doi.org/10.1029/2020JD032657>
- 819 Liu, D., Whitehead, J., Alfarra, M. R., Reyes-villegas, E., Spracklen, D. V., Reddington, C. L., et al. (2017). Black-
820 carbon absorption enhancement in the atmosphere determined by particle mixing state. *Nature Geoscience*,
821 10(3), 184–188. <https://doi.org/10.1038/NGEO2901>
- 822 Liu, D., He, C., Schwarz, J. P., & Wang, X. (2020). Lifecycle of light-absorbing carbonaceous aerosols in the
823 atmosphere. *Npj Climate and Atmospheric Science*, 3(40). <https://doi.org/10.1038/s41612-020-00145-8>
- 824 Liu, J., Bergin, M., Guo, H., King, L., Kotra, N., Edgerton, E., & Weber, R. J. (2013). Size-resolved measurements of
825 brown carbon in water and methanol extracts and estimates of their contribution to ambient fine-particle light
826 absorption. *Atmospheric Chemistry and Physics*, 13(24), 12389–12404. [https://doi.org/10.5194/acp-13-12389-
827 2013](https://doi.org/10.5194/acp-13-12389-2013)
- 828 Liu, S., Aiken, A. C., Gorkowski, K., Dubey, M. K., Cappa, C. D., Williams, L. R., et al. (2015). Enhanced light
829 absorption by mixed source black and brown carbon particles in UK winter. *Nature Communications*, 6, 8435.
830 <https://doi.org/10.1038/ncomms9435>
- 831 Marple, V. A., Rubow, K. L., & Behm, S. M. (1991). A microorifice uniform deposit impactor (moudi): Description,
832 calibration, and use. *Aerosol Science and Technology*, 14(4), 434–436.
833 <https://doi.org/10.1080/02786829108959504>
- 834 McConnell, J. R., Edwards, R., Kok, L. G., Flanner, M. G., Zender, C. S., Saltzman, E. S., et al. (2007). 20th-Century
835 Industrial Black Carbon Emissions Altered Arctic Climate Forcing. *Science*, 317(5843), 1381–1384.
836 <https://doi.org/10.1126/science.1144856>
- 837 Moharreri, A., Craig, L., Dubey, P., Rogers, D. C., & Dhaniyala, S. (2014). Aircraft testing of the new Blunt-body
838 Aerosol Sampler (BASE). *Atmospheric Measurement Techniques*, 7(9), 3085–3093.
839 <https://doi.org/10.5194/amt-7-3085-2014>



- 840 Neumann, J. E., Amend, M., Anenberg, S., Kinney, P. L., Sarofim, M., Martinich, J., et al. (2021). Estimating PM_{2.5}-
841 related premature mortality and morbidity associated with future wildfire emissions in the western US.
842 *Environmental Research Letters*, 16(3). <https://doi.org/10.1088/1748-9326/abe82b>
- 843 Onasch, T. B., Massoli, P., Keabian, P. L., Hills, F. B., Bacon, F. W., & Freedman, A. (2015). Single scattering
844 albedo monitor for airborne particulates. *Aerosol Science and Technology*, 49(4), 267–279.
845 <https://doi.org/10.1080/02786826.2015.1022248>
- 846 Orsini, D. A., Ma, Y., Sullivan, A., Sierau, B., Baumann, K., & Weber, R. J. (2003). Refinements to the particle-into-
847 liquid sampler (PILS) for ground and airborne measurements of water soluble aerosol composition. *Atmospheric*
848 *Environment*, 37(9–10), 1243–1259. [https://doi.org/10.1016/S1352-2310\(02\)01015-4](https://doi.org/10.1016/S1352-2310(02)01015-4)
- 849 Palm, B. B., Peng, Q., Fredrickson, C. D., Lee, B. H., Garofalo, L. A., Pothier, M. A., et al. (2020). Quantification of
850 organic aerosol and brown carbon evolution in fresh wildfire plumes. *Proceedings of the National Academy of*
851 *Sciences of the United States of America*, 117(47), 29469–29477. <https://doi.org/10.1073/pnas.2012218117>
- 852 Peltier, R. E., Weber, R. J., & Sullivan, A. P. (2007). Investigating a liquid-based method for online organic carbon
853 detection in atmospheric particles. *Aerosol Science and Technology*, 41(12), 1117–1127.
854 <https://doi.org/10.1080/02786820701777465>
- 855 Peng, J., Hu, M., Guo, S., Du, Z., Zheng, J., Shang, D., et al. (2016). Markedly enhanced absorption and direct radiative
856 forcing of black carbon under polluted urban environments. *Proceedings of the National Academy of Sciences*
857 *of the United States of America*, 113(16), 4266–4271. <https://doi.org/10.1073/pnas.1602310113>
- 858 Peng, Q., Palm, B. B., Melander, K. E., Lee, B. H., Hall, S. R., Ullmann, K., et al. (2020). HONO Emissions from
859 Western U.S. Wildfires Provide Dominant Radical Source in Fresh Wildfire Smoke. *Environmental Science and*
860 *Technology*, 54(10), 5954–5963. <https://doi.org/10.1021/acs.est.0c00126>
- 861 Permar, W., Wang, Q., Selimovic, V., Wielgasz, C., Yokelson, R. J., Hornbrook, R. S., et al. (2021). Emissions of
862 Trace Organic Gases From Western U.S. Wildfires Based on WE-CAN Aircraft Measurements. *Journal of*
863 *Geophysical Research: Atmospheres*, 126(11). <https://doi.org/10.1029/2020JD033838>
- 864 Pokhrel, R. P., Wagner, N. L., Langridge, J. M., Lack, D. A., Jayarathne, T., Stone, E. A., et al. (2016).
865 Parameterization of single-scattering albedo (SSA) and absorption Ångström exponent (AAE) with EC/OC for
866 aerosol emissions from biomass burning. *Atmospheric Chemistry and Physics*, 16(15), 9549–9561.
867 <https://doi.org/10.5194/acp-16-9549-2016>
- 868 Pokhrel, R. P., Beamesderfer, E. R., Wagner, N. L., Langridge, J. M., Lack, D. A., Jayarathne, T., et al. (2017).
869 Relative importance of black carbon, brown carbon, and absorption enhancement from clear coatings in biomass
870 burning emissions. *Atmospheric Chemistry and Physics*, 17(8), 5063–5078. [https://doi.org/10.5194/acp-17-](https://doi.org/10.5194/acp-17-5063-2017)
871 [5063-2017](https://doi.org/10.5194/acp-17-5063-2017)
- 872 Rosenwaig, A. (1980). *Photoacoustics and photoacoustic spectroscopy*. *Annual Review of Biophysics and*
873 *Bioengineering*, 9, 31–54. <https://doi.org/10.1146/annurev.bb.09.060180.000335>
- 874 Saleh, R., Robinson, E. S., Tkacik, D. S., Ahern, A. T., Liu, S., Aiken, A. C., et al. (2014). Brownness of organics in
875 aerosols from biomass burning linked to their black carbon content. *Nature Geoscience*, 7(9), 647–650.
876 <https://doi.org/10.1038/ngeo2220>



- 877 Sarangi, C., Qian, Y., Rittger, K., Leung, R. L., Chand, D., Bormann, K. J., & Painter, T. H. (2020). Dust dominates
878 high-altitude snow darkening and melt over high-mountain Asia. *Nature Climate Change*, (October), 1–7.
879 <https://doi.org/10.1038/s41558-020-00909-3>
- 880 Schnaiter, M., Horvath, H., Möhler, O., Naumann, K. H., Saathoff, H., & Schöck, O. W. (2003). UV-VIS-NIR spectral
881 optical properties of soot and soot-containing aerosols. *Journal of Aerosol Science*, 34(10), 1421–1444.
882 [https://doi.org/10.1016/S0021-8502\(03\)00361-6](https://doi.org/10.1016/S0021-8502(03)00361-6)
- 883 Schnaiter, M., Linke, C., Möhler, O., Naumann, K. H., Saathoff, H., Wagner, R., et al. (2005). Absorption
884 amplification of black carbon internally mixed with secondary organic aerosol. *Journal of Geophysical Research*
885 *D: Atmospheres*, 110(19), 1–11. <https://doi.org/10.1029/2005JD006046>
- 886 Schwarz, J. P., Gao, R. S., Fahey, D. W., Thomson, D. S., Watts, L. A., Wilson, J. C., et al. (2006). Single-particle
887 measurements of midlatitude black carbon and light-scattering aerosols from the boundary layer to the lower
888 stratosphere. *Journal of Geophysical Research*, 111, D16207. <https://doi.org/10.1029/2006JD007076>
- 889 Subramanian, R., Kok, G. L., Baumgardner, D., Clarke, A., Shinozuka, Y., Campos, T. L., et al. (2010). Black carbon
890 over Mexico: The effect of atmospheric transport on mixing state, mass absorption cross-section, and BC/CO
891 ratios. *Atmospheric Chemistry and Physics*, 10(1), 219–237. <https://doi.org/10.5194/acp-10-219-2010>
- 892 Sullivan, A. P., Pokhrel, R. P., Shen, Y., Murphy, S. M., Toohey, D. W., Campos, T., Lindaas, J., Fischer, E. V., and
893 Collett Jr., J. L. (2022). Examination of Brown Carbon Absorption from Wildfires in the Western U.S. During
894 the WE-CAN Study. *Atmospheric Chemistry and Physics*, 22(20), 13389–13406. <https://doi.org/10.5194/acp-22-13389-2022>
- 895
- 896 Sun, Y., Zhang, Q., Zheng, M., Ding, X., Edgerton, E. S., & Wang, X. (2011). Characterization and source
897 apportionment of water-soluble organic matter in atmospheric fine particles (PM_{2.5}) with high-resolution
898 aerosol mass spectrometry and GC-MS. *Environmental Science and Technology*, 45(11), 4854–4861.
899 <https://doi.org/10.1021/es200162h>
- 900 Szopa, S., V. Naik, B. Adhikary, P. Artaxo, T. Berntsen, W.D. Collins, S. et al. (2021): Short-Lived Climate Forcers.
901 In *Climate Change 2021: The Physical Science Basis. Contribution of Working Group I to the Sixth Assessment*
902 *Report of the Intergovernmental Panel on Climate Change*. Cambridge University Press, Cambridge, United
903 Kingdom and New York, NY, USA, pp. 817–922, <https://doi.org/10.1017/9781009157896.008>
- 904 Tasoglou, A., Louvaris, E., Florou, K., Liangou, A., Karnezi, E., Kaltsonoudis, C., et al. (2020). Aerosol light
905 absorption and the role of extremely low volatility organic compounds. *Atmospheric Chemistry and Physics*,
906 20(19), 11625–11637. <https://doi.org/10.5194/acp-20-11625-2020>
- 907 Taylor, J. W., Wu, H., Szpek, K., Bower, K., Crawford, I., Flynn, M. J., et al. (2020). Absorption closure in highly
908 aged biomass burning smoke. *Atmospheric Chemistry and Physics*, 20(19), 11201–11221.
909 <https://doi.org/10.5194/acp-20-11201-2020>
- 910 Wei, Y., Ma, L., Cao, T., Zhang, Q., Wu, J., Buseck, P. R., & Thompson, J. E. (2013). Light scattering and extinction
911 measurements combined with laser-induced incandescence for the real-time determination of soot mass
912 absorption cross section. *Analytical Chemistry*, 85(19), 9181–9188. <https://doi.org/10.1021/ac401901b>



- 913 Westerling, A. L., Hidalgo, H. G., Cayan, D. R., & Swetnam, T. W. (2006). Warming and Earlier Spring Increase
914 Western U. S. Forest Wildfire Activity. *Science*, 313(5789), 940–943. <https://doi.org/10.1126/science.1128834>
- 915 Williams, E. L., & Grosjean, D. (1990). Removal of Atmospheric Oxidants with Annular Denuders. *Environmental
916 Science and Technology*, 24(6), 811–814. <https://doi.org/10.1021/es00076a002>
- 917 Wonaschütz, A., Hitzengerger, R., Bauer, H., Pournesmaeil, P., Klatzer, B., Caseiro, A., & Puxbaum, H. (2009).
918 Application of the integrating sphere method to separate the contributions of brown and black carbon in
919 atmospheric aerosols. *Environmental Science and Technology*, 43(4), 1141–1146.
920 <https://doi.org/10.1021/es8008503>
- 921 Yue, X., Mickley, L. J., Logan, J. A., & Kaplan, J. O. (2013). Ensemble projections of wildfire activity and
922 carbonaceous aerosol concentrations over the western United States in the mid-21st century. *Atmospheric
923 Environment*, 77, 767–780. <https://doi.org/10.1016/j.atmosenv.2013.06.003>
- 924 Zeng, L., Zhang, A., Wang, Y., Wagner, N. L., Katich, J. M., Schwarz, J. P., et al. (2020). Global Measurements of
925 Brown Carbon and Estimated Direct Radiative Effects. *Geophysical Research Letters*, 47(13).
926 <https://doi.org/10.1029/2020GL088747>
- 927 Zeng, L., Sullivan, A. P., Washenfelder, R. A., Dibb, J., Scheuer, E., Campos, T. L., et al. (2021). Assessment of
928 online water-soluble brown carbon measuring systems for aircraft sampling. *Atmospheric Measurement
929 Techniques*, 14(10), 6357–6378. <https://doi.org/10.5194/amt-14-6357-2021>
- 930 Zeng, L., Dibb, J., Scheuer, E., Katich, J. M., Schwarz, J. P., Bourgeois, I., et al. (2022). Characteristics and Evolution
931 of Brown Carbon in Western United States Wildfires. *Atmospheric Chemistry and Physics*, 22, 8009–8036.
932 <https://doi.org/10.5194/acp-22-8009-2022>
- 933 Zhang, L., Segal-Rozenhaimer, M., Che, H., Dang, C., Sedlacek III, A. J., Lewis, E. R., Dobracki, A., Wong, J. P. S.,
934 Formenti, P., Howell, S. G., and Nenes, A.: Light Absorption by Brown Carbon over the South-East Atlantic
935 Ocean, *Atmos. Chem. Phys. Discuss.* [preprint], <https://doi.org/10.5194/acp-2021-1000>, in review, 2022.
- 936 Zhang, Y., Forrister, H., Liu, J., Dibb, J., Anderson, B., Schwarz, J. P., et al. (2017). Top-of-atmosphere radiative
937 forcing affected by brown carbon in the upper troposphere. *Nature Geoscience*, 10(7), 486–489.
938 <https://doi.org/10.1038/ngeo2960>